



HAL
open science

The Gaia -ESO survey: Mixing processes in low-mass stars traced by lithium abundance in cluster and field stars

L. Magrini, Nadège Lagarde, Corinne Charbonnel, E. Franciosini, S. Randich, R. Smiljanic, G. Casali, C. Viscasillas Vázquez, L. Spina, K. Biazzo, et al.

► To cite this version:

L. Magrini, Nadège Lagarde, Corinne Charbonnel, E. Franciosini, S. Randich, et al.. The Gaia - ESO survey: Mixing processes in low-mass stars traced by lithium abundance in cluster and field stars. *Astronomy and Astrophysics - A&A*, 2021, 651, pp.A84. 10.1051/0004-6361/202140935 . hal-03434408

HAL Id: hal-03434408


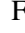


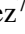



<https://hal.science/hal-03434408>

Submitted on 18 Nov 2021

HAL is a multi-disciplinary open access archive for the deposit and dissemination of scientific research documents, whether they are published or not. The documents may come from teaching and research institutions in France or abroad, or from public or private research centers.

L'archive ouverte pluridisciplinaire **HAL**, est destinée au dépôt et à la diffusion de documents scientifiques de niveau recherche, publiés ou non, émanant des établissements d'enseignement et de recherche français ou étrangers, des laboratoires publics ou privés.

The *Gaia*-ESO survey: Mixing processes in low-mass stars traced by lithium abundance in cluster and field stars^{★,★★}

L. Magrini¹, N. Lagarde², C. Charbonnel^{3,4}, E. Franciosini¹, S. Randich¹, R. Smiljanic⁵, G. Casali^{1,6}, C. Viscasillas Vázquez⁷, L. Spina⁸, K. Biazzo⁹, L. Pasquini¹⁰, A. Bragaglia¹¹, M. Van der Swaelmen¹, G. Tautvaišienė⁷, L. Inno^{12,13}, N. Sanna¹, L. Prisinzano¹⁴, S. Degl'Innocenti^{15,16}, P. Prada Moroni^{15,16}, V. Roccatagliata^{15,16,1}, E. Tognelli^{15,16}, L. Monaco¹⁷, P. de Laverny¹⁸, E. Delgado-Mena¹⁹, M. Baratella^{20,8}, V. D'Orazi⁸, A. Vallenari⁸, A. Gonneau²¹, C. Worley²¹, F. Jiménez-Esteban²², P. Jofre²³, T. Bensby²⁴, P. François²⁵, G. Guiglion²⁶, A. Bayo^{27,28}, R. D. Jeffries²⁹, A. S. Binks²⁹, G. Gilmore²¹, F. Damiani¹⁴, A. Korn²⁴, E. Pancino^{1,30}, G. G. Sacco¹, A. Hourihane²¹, L. Morbidelli¹, and S. Zaggia⁸

(Affiliations can be found after the references)

Received 30 March 2021 / Accepted 5 May 2021

ABSTRACT

Aims. We aim to constrain the mixing processes in low-mass stars by investigating the behaviour of the Li surface abundance after the main sequence. We take advantage of the data from the sixth internal data release of *Gaia*-ESO, IDR6, and from the *Gaia* Early Data Release 3, EDR3s. **Methods.** We selected a sample of main-sequence, sub-giant, and giant stars in which the Li abundance is measured by the *Gaia*-ESO survey. These stars belong to 57 open clusters with ages from 130 Myr to about 7 Gyr and to Milky Way fields, covering a range in [Fe/H] between ~ -1.0 and $\sim +0.5$ dex, with few stars between ~ -1.0 and ~ -2.5 dex. We studied the behaviour of the Li abundances as a function of stellar parameters. We inferred the masses of giant stars in clusters from the main-sequence turn-off masses, and for field stars through comparison with stellar evolution models using a maximum likelihood technique. We compared the observed Li behaviour in field giant stars and in giant stars belonging to individual clusters with the predictions of a set of classical models and of models with mixing induced by rotation and thermohaline instability. **Results.** The comparison with stellar evolution models confirms that classical models cannot reproduce the observed lithium abundances in the metallicity and mass regimes covered by the data. The models that include the effects of both rotation-induced mixing and thermohaline instability account for the Li abundance trends observed in our sample in all metallicity and mass ranges. The differences between the results of the classical models and of the rotation models largely differ (up to 2 dex), making lithium the best element with which to constrain stellar mixing processes in low-mass stars. We discuss the nature of a sample of Li-rich stars.

Conclusions. We demonstrate that the evolution of the surface abundance of Li in giant stars is a powerful tool for constraining theoretical stellar evolution models, allowing us to distinguish the effect of different mixing processes. For stars with well-determined masses, we find a better agreement of observed surface abundances and models with rotation-induced and thermohaline mixing. Rotation effects dominate during the main sequence and the first phases of the post-main-sequence evolution, and the thermohaline induced mixing after the bump in the luminosity function.

Key words. stars: abundances – stars: evolution – open clusters and associations: general

1. Introduction

Big Bang nucleosynthesis mostly produced H and He, together with a small amount of the lithium-7 isotope (hereafter Li; e.g. Coc et al. 2004; Galli & Palla 2013; Olive 2013; Pitrou et al. 2018). However, the Li that is observed in the present-day Universe is only in part the Li that was originally produced during the Big Bang because its abundance is modified by a number of constructive and destructive processes that make Li one of the elements with the most complex history (e.g. Matteucci et al. 1995; Romano et al. 2001; Travaglio et al. 2001; Prantzos 2012; Bensby & Lind 2018; Grisoni et al. 2019; Randich et al. 2020; Smiljanic 2020; Randich & Magrini 2021).

* Full Tables 2, A.1–A3 are only available at the CDS via anonymous ftp to cdsarc.u-strasbg.fr (130.79.128.5) or via <http://cdsarc.u-strasbg.fr/viz-bin/cat/J/A+A/651/A84>

** Based on observations collected with the FLAMES instrument at VLT/UT2 telescope (Paranal Observatory, ESO, Chile), for the *Gaia*-ESO Large Public Spectroscopic Survey (188.B-3002, 193.B-0936, 197.B-1074).

One of the difficulties in tracing the history of cosmic Li is that with the exception of the early pre-main-sequence (PMS) phases, stars rarely exhibit the original Li with which they formed. This fragile element is destroyed by proton captures in stellar interiors when the temperature is $\sim 2.5 \times 10^6$ K or higher. Depending on the mass and metallicity of the star, photospheric Li can be significantly depleted already on the PMS during the proto-stellar accretion phase (Tognelli et al. 2020) and along the Hayashi track, and/or on the main sequence (MS) as a result of several mechanisms that have the potential of transporting the photospheric material into hotter layers where Li can be burned: atomic diffusion, overshooting, rotation-induced mixing, internal gravity waves, and other types of magneto-hydrodynamical instabilities that are not included in the so-called classical evolution models (Michaud 1986; Charbonneau & Michaud 1990; Schramm et al. 1990; Richard et al. 1996; Deliyannis et al. 2000; Denissenkov & Tout 2003; Talon & Charbonnel 2010; Eggenberger et al. 2012; Castro et al. 2016; Somers & Pinsonneault 2016; Baraffe et al. 2017; Deal et al. 2021; Dumont et al. 2021).

After the MS, convection sinks inside the stars and brings material to the surface that has been partially nuclear-processed in the stellar interior. This enriches the external layers in ^{13}C , ^{14}N , and ^3He , and dilutes Li. According to the classical model by Iben (1967), during this so-called first dredge-up event (FDU), the surface Li abundance decreases by a factor from 30 to 60, depending on the stellar mass and metallicity. Starting from the current interstellar medium abundance of $A(\text{Li})^1 = 3.3$ dex (the value found in Solar System meteorites and considered the reference limit for Population I dwarf stars; Asplund et al. 2009), the Li abundance of red giant stars is thus expected to decrease to a value $A(\text{Li}) \sim 1.5$ dex at least. Models that include some of the transport processes listed above that already act on the MS predict lower post-FDU values of lithium abundances. These models better agree with the observations of subgiant and giant stars (i.e. Li depletion appears at hotter effective temperature and is higher than in classical models; see e.g. Brown et al. 1989; Balachandran 1995; Palacios et al. 2003; Mallik et al. 2003; Pasquini et al. 2004; Lèbre et al. 2006; Gonzalez et al. 2009; Anthony-Twarog et al. 2009; Charbonnel et al. 2020).

Finally, classical models do not predict any decreasing trend of the Li abundance in the subsequent evolutionary phases, although Li is observed to drop again after the luminosity bump on the red giant branch (RGB; e.g. Charbonnel et al. 1998; Gratton et al. 2000; Lind et al. 2009). This is likely caused by the activation of thermohaline (double diffusive) instability, which could also affect the carbon and nitrogen abundances (e.g. Charbonnel & Zahn 2007; Denissenkov et al. 2009; Charbonnel & Lagarde 2010; Lattanzio et al. 2015).

While some non-classical stellar models can reproduce the main Li trends described above, they still have serious shortcomings. For example, they fail to simultaneously reproduce the internal rotation profiles of sub-giant and giant stars as depicted by asteroseismology (e.g. Marques et al. 2013; Ceillier et al. 2013; Eggenberger et al. 2017, 2019). In addition, different prescriptions for thermohaline mixing are required to explain the surface abundance of Li and C in low-metallicity bright red giant stars (e.g. Angelou et al. 2015; Henkel et al. 2017). The difficulty is that macroscopic magnetohydrodynamic (MHD) transport processes act on a broad range of spatial and time scales that cannot be handled numerically when secular evolution is computed (e.g. Mathis 2013). One-dimensional stellar models thus rely on simplified prescriptions for turbulence and magneto-hydrodynamic instabilities that are, in the best case, “educated” based on numerical and laboratory experiments, which are, however, still far from reproducing stellar interior conditions (e.g. Richard & Zahn 1999; Palmerini et al. 2011; Prat & Lignières 2013; Prat et al. 2015; Garaud & Kulenthirarajah 2016; Mathis et al. 2018; Sengupta & Garaud 2018; Garaud 2021).

In this framework, observations of large samples of stars with available Li abundances provide fundamental constraints to models. However, most studies focused on field stars and only included small numbers of star clusters (see e.g. Lambert et al. 1980; Balachandran 1990; Pasquini et al. 2004; Lind et al. 2009; Smiljanic et al. 2009; Canto Martins et al. 2011). So far, a homogeneous analysis of Li in both field and cluster populations is lacking, even in large spectroscopic surveys, such as the GALactic Archaeology with HERMES survey (GALAH; Buder et al. 2021).

In the present work, we take advantage of the *Gaia*-ESO database (Gilmore et al. 2012; Randich et al. 2013) for the sixth

internal data release (IDR6), which includes homogeneously determined Li abundances in stars of open clusters and in the field. With these data, we investigate the Li abundance evolution after the MS over a wide range of $[\text{Fe}/\text{H}]$ and stellar masses. In particular, for clusters, metallicity and age, and consequently the masses of their stars at the main sequence turn-off (MSTO) and RGB, can be estimated more accurately than for field stars, therefore they allow a more accurate comparison with the results of theoretical models. In addition, the observed star clusters are usually younger than field stars, which allows us to map higher mass ranges.

The paper is structured as follows. In Sect. 2 we present the abundance analysis and the sample selection. In Sect. 3 we compare the *Gaia*-ESO IDR6 results with other catalogues. In Sect. 4 we study the behaviour of Li abundances along the RGB in field stars with masses determined with a maximum likelihood method using a large and homogeneous grid of stellar models. We also study this in members of individual star clusters. We compare our data with model predictions and discuss the effect of rotation-induced mixing and thermohaline instability. In Sect. 5 we identify Li-rich giants, discuss their properties, and the effect of stellar rotation. Finally, in Sect. 6 we give our summary and conclusions.

2. Abundance analysis and sample selection

2.1. Li abundance determination

We used data from IDR6 of the *Gaia*-ESO Survey, derived from the UVES spectra with resolving power $R = 47\,000$ and spectral range 480.0–680.0 nm, and the GIRAFFE HR15N spectra ($R \sim 19\,000$), covering the wavelength range 647–679 nm. Both types of spectra were reduced and analysed by the *Gaia*-ESO consortium. The data reduction and analysis process have been described in several papers (see e.g. Sacco et al. 2014; Smiljanic et al. 2014; Jackson et al. 2015; Lanzafame et al. 2015); we recall the main steps here. The pipelines for data reduction, as well as radial and rotational velocity determinations, are run at INAF-Arcetri for UVES (Sacco et al. 2014) using the FLAMES-UVES ESO public pipeline, and at the Cambridge Astronomy Survey Unit (CASU) for GIRAFFE. The spectral analysis is shared among different working groups (WGs), to which spectra are assigned on the basis of the stellar type, instrument, and setup. The data discussed in this paper were analysed by WG10, WG11, and WG12, which are in charge of the analysis of the UVES and GIRAFFE spectra of F , G , K (and M for WG12) stars in the field of the Milky Way (MW) and in open clusters. The spectra in each WG are analysed with a strategy based on multiple pipelines, as described in Worley et al. (in prep.), Smiljanic et al. (2014), and Lanzafame et al. (2015) for WG10, WG11, and WG12, respectively. Finally, the results from the different WGs are homogenised using a database of calibrators, such as benchmark stars and open or globular clusters selected following the calibration strategy by Pancino et al. (2017) and adopted for the homogenisation by WG15 (Hourihane et al., in prep.). The recommended parameters and abundances are distributed in the IDR6 catalogue, which includes those used in the present work: atmospheric stellar parameters T_{eff} , $\log g$, and/or γ , the surface gravity index based on the ratios of high-gravity and low-gravity lines in the spectral region 675.0–678.0 nm and defined in Damiani et al. (2014), metallicity $[\text{Fe}/\text{H}]$, lithium abundances (measurements or upper limits), radial velocities (RVs), and projected equatorial rotational velocities ($v \sin i$).

¹ $A(\text{Li}) = \log\left(\frac{X(\text{Li})}{X(\text{H})} \cdot \frac{A_{\text{H}}}{A_{\text{Li}}}\right) + 12$, where X and A are the mass fraction and the atomic mass.

The lithium abundance is measured from the doublet lines at 670.8 nm. At the resolution of GIRAFFE, this line is blended with the nearby FeI line at 670.74 nm, but the two components can be clearly separated in UVES. In IDR6, the Li abundances from UVES and GIRAFFE spectra were derived in a homogeneous way. Lithium equivalent widths (EWs) were measured by Gaussian fitting of the lithium doublet components and the FeI line, and then converted into abundances using a set of ad hoc curves of growth (Franciosi et al., in prep.) that were specifically derived for the *Gaia*-ESO survey with a grid of synthetic spectra computed as in de Laverny et al. (2012) and Guiglion et al. (2016) and based on the MARCS model atmospheres in the following ranges: $3000 \leq T_{\text{eff}} \leq 8000$ K, $0.5 \leq \log g \leq 5.0$, $-2.50 \leq [\text{Fe}/\text{H}] \leq +0.50$, and $-1.0 \leq A(\text{Li}) \leq 4.0$. In the case of GIRAFFE, where only the total blended Li+Fe EW can be measured, the Li-only EW was first computed by applying a correction for the Fe blend, measured on the same synthetic spectra as were used to derive the curves of growth. When the line is not visible (or just barely visible), an upper limit to the EW, equal to the uncertainty, or to the measured EW if higher, is given.

The *Gaia*-ESO abundances are determined in the local thermodynamic equilibrium (LTE) approximation. We estimate the typical effect on Li abundances introduced by the LTE approximation in one dimensional (1D) hydrostatic atmospheres following Wang et al. (2021), who computed a three-dimensional non local thermodynamic equilibrium (3D NLTE) Li grid spanning the parameter range for FGK-type dwarfs and giants. The 3D NLTE corrections can increase or decrease $A(\text{Li})$ by a few tenths of a dex in the typical ranges of parameters of our sample of giant stars. We compute them for the sample of stars for which all stellar parameters are available, using the code and grids provided by Wang et al. (2021). In Figs. 1 and 2 we show the effect of the correction $\Delta(A(\text{Li})_{3\text{D-NLTE}} - A(\text{Li})_{1\text{D-LTE}})$ in the Kiel diagram, and as a function of T_{eff} for field stars and open clusters, respectively. For both samples the effect is within ± 0.1 dex, depending on T_{eff} , and it is almost negligible for MSTO stars and for giant stars hotter than 4200 K. In the next sections, we adopt the 1D LTE *Gaia*-ESO Li abundances, which are also available for stars for which $\log g$ has not been determined.

2.2. Sample selection

We analysed the *Gaia*-ESO IDR6 sample of MS, sub-giant, and giant stars with available Li determination, focusing on the post-MS evolution of lithium surface abundances. The spectral ranges of the HR15N and U580 setups allowed us to measure the Li doublet lines. In particular, the GIRAFFE setup HR15N is dedicated in *Gaia*-ESO to the study of stars in open clusters. However, because the target selection of member stars in clusters observed with GIRAFFE is unbiased and inclusive, many non-member contaminants, including in particular giant stars, are present in the *Gaia*-ESO database. The contamination by distant field giants is even more important in the field of view of the youngest star clusters because the colours and hence position in the colour-magnitude diagrams that were used for target selection are similar. We took advantage of this favourable configuration to build a large sample of high-resolution spectra of field and cluster stars with Li measurements in a wide range of metallicity. We broadly define giant stars as those with $T_{\text{eff}} \leq 5400$ K and $\log g \leq 3.8$ (or $\gamma \geq 0.98$, if $\log g$ is not available). The remaining sample includes sub-giants (with $5400 \leq T_{\text{eff}} \leq 6000$ K and $\log g \leq 4$, although the limits are difficult to determine precisely) and MS stars.

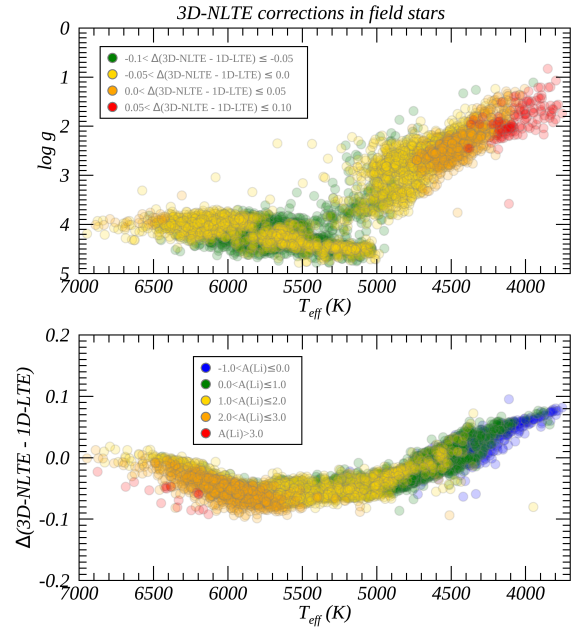


Fig. 1. Upper panel: Kiel diagram of the field stars, colour-coded by $\Delta(A(\text{Li})_{3\text{D-NLTE}} - A(\text{Li})_{1\text{D-LTE}})$. Lower panel: $\Delta(A(\text{Li})_{3\text{D-NLTE}} - A(\text{Li})_{1\text{D-LTE}})$ vs. T_{eff} for field stars colour-coded by $A(\text{Li})$.

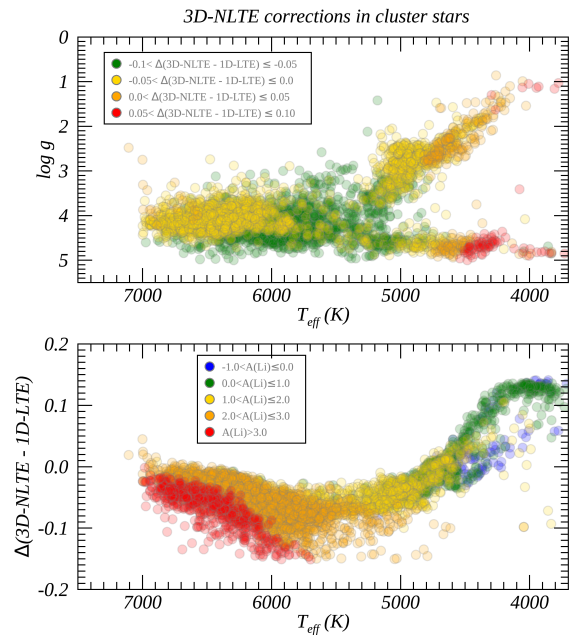


Fig. 2. Same as Fig. 1, but for stars in open clusters.

2.2.1. Open cluster sample

The *Gaia*-ESO IDR6 contains 86 open clusters (87 considering the two clusters in NGC 2451A and B, Randich et al. 2018), which also include calibration clusters and those retrieved from the ESO archive. Our analysis considered 57 clusters (over 62) with age > 120 Myr hosting evolved giant stars for which the lithium abundance is available, considering our constraints on stellar parameters and Li abundances. We excluded 5 clusters in which no giant stars were observed and one with a very poor membership (Loden 165). The histogram of the age distribution of the selected clusters, determined homogeneously by

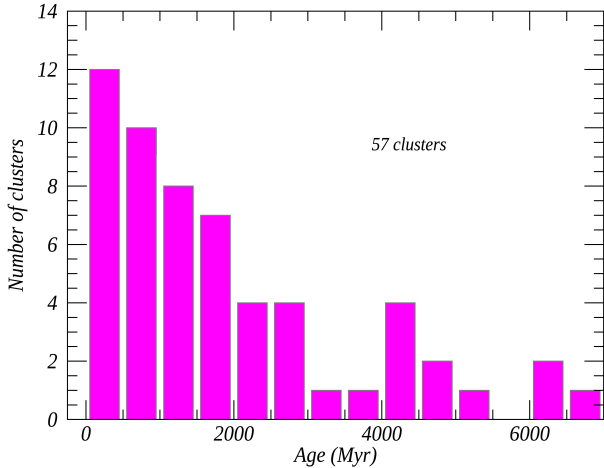


Fig. 3. Histogram of the ages from CG20 for our sample of open clusters (age ≥ 130 Myr). The bin size is 0.5 Gyr.

Cantat-Gaudin et al. (2020, hereafter, CG20), is shown in Fig. 3. The cluster parameters are presented in Table A.1, including the cluster name, age, distance, and galactocentric radius from CG20, mean radial velocity (RV) and [Fe/H] from the UVES members in *Gaia*-ESO IDR6, MSTO mass derived from the Parsec isochrones that were used by CG20 for age determination (Bressan et al. 2012), and the selected isochrones.

The ages of our sample clusters span from 130 Myr to about 7 Gyr. For the clusters containing more than 20 targets, the member stars were selected by performing a simultaneous fit of the *Gaia*-ESO RVs and of the parallaxes and proper motions from *Gaia* EDR3 (Gaia Collaboration 2021). For this aim, we extended the method described by Franciosini et al. (2018) and Roccatagliata et al. (2018), adding the RV as fourth (independent) parameter. For each cluster, the distribution was fitted with two multivariate Gaussians, one for the cluster and one for the field, taking measurement errors and the *Gaia* covariance matrix into account. When strong contamination from the field was present, we first discarded the objects located at more than 5σ from a first-guess average centroid for the cluster parallax and proper motions. *Gaia* astrometry was only used in the fit if the renormalised unit weight error (RUWE), a statistical indicator of the quality of the data, was ≤ 1.4 . An example of the fit is shown in Fig. 4 for the case of NGC 2158. We then computed a membership probability for each star in the usual way, that is, dividing the cluster distribution by the total distribution, and selected objects with $P > 0.8$ as members. For the remaining clusters with fewer than 20 targets, to which this method cannot be applied, we first derived the peak and standard deviation of the RV distribution, and selected stars within 2σ of the peak. We then computed the average parallax and proper motion and the corresponding standard deviations for the selected stars, and we further excluded those differing more than 2σ from the average values. We compared this selection with that of CG20, finding excellent agreement in general. With our selection we can add some members for the fainter stars or in crowded fields for which CG20 did not provide a membership probability.

We made a further selection on giant stars, based on the errors on the stellar parameters ($\text{error}(T_{\text{eff}}) < 100$ K, $\text{error}(\log g) < 0.2$, $\text{error}([\text{Fe}/\text{H}]) < 0.15$), and including only stars with measured lithium abundances with an error on $A(\text{Li})$ lower than 0.25 dex or upper limits. We relaxed the selection on the error on $A(\text{Li})$ for Li-rich giant stars. These are defined, as in Casey et al. (2016) and Smiljanic et al. (2018), as stars

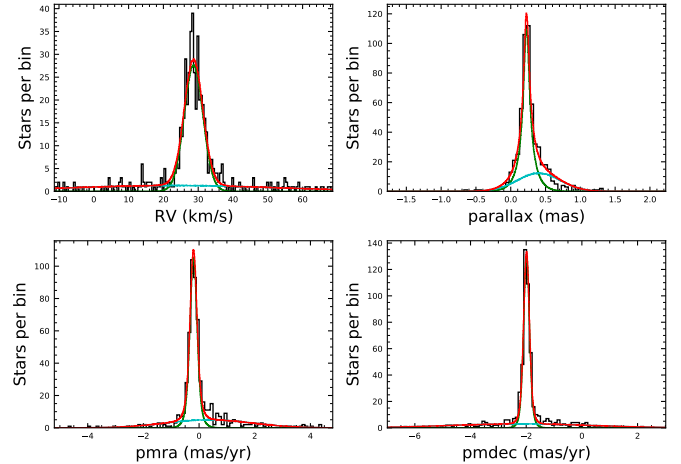


Fig. 4. Result of the multivariate Gaussian fit of the distribution of RV, parallax, and proper motions (in RA and Dec) for NGC 2158. The total distribution is shown in red, and the green and cyan lines show the cluster and field components, respectively.

with $3800 \text{ K} \leq T_{\text{eff}} \leq 5000 \text{ K}$, $\log g \leq 3.5$ – or $\gamma \geq 0.98$, and $\log(L/L_{\odot}) \geq 1$ dex for star selected as giants based on their γ index, and $A(\text{Li}) \geq 2.0$ dex, for which we did not apply any error cut. The Hertzsprung-Russell diagram (hereafter HRD) and the Kiel ($\log g - T_{\text{eff}}$) diagram of the selected members of open clusters are displayed in Fig. 5. The final number of considered cluster members is 4212 (see Table 1), about 18% of which are giant stars. The stellar parameters, $A(\text{Li})$ (measurements and upper limits), and MSTO masses for the adopted sample of cluster stars are given in Table A.2.

2.2.2. Field star sample

For the sample of field stars, we selected stars in two different ways, depending on the WG that analysed them. The first selection allowed us to identify the observed field stars as non-members of young clusters with age ≤ 120 Myr, which were analysed by WG12. To select them, we inverted the selection applied by Bravi et al. (2018), keeping stars with $T_{\text{eff}} < 5400$ K and either $\gamma > 0.98$, for those observed with GIRAFFE, or $\log g < 3.8$ for those observed with UVES. For $4800 \text{ K} < T_{\text{eff}} \leq 5400 \text{ K}$, we selected stars with $\gamma > 0.98$, while for stars with $T_{\text{eff}} \leq 4800$ K, we adopted the selection $\gamma \geq 1.22 - 5 \times 10^{-5} \times T_{\text{eff}}$ to avoid contamination by the coolest MS and PMS stars. The selections in the γ vs. T_{eff} and $\log g$ vs. T_{eff} diagrams are illustrated in the top and bottom panels of Fig. 6, respectively. In the figure we also indicate the Li-rich red giant stars with $A(\text{Li}) \geq 2.0$ dex.

The second selection criterion allowed us to select (i) field stars that are non-members of the old and intermediate-age open clusters (age > 120 Myr): in this selection, we took all stars into account that were not selected as cluster members on the basis of their radial velocities, proper motions, and parallaxes; and (ii) the stars observed in the *Gaia*-ESO field samples by selecting the GES_FLD keywords related to the field stars (GES_MW for general Milky Way fields, GES_MW_BL for fields in the direction of the Galactic bulge, GES_K2 for stars observed in Kepler2 (K2) fields, GES_CR for stars observed in CoRoT fields). We combined the two samples of field stars, performing a further selection on stellar parameter uncertainties, as was done for the sample of stars in open clusters. The results of the selection are shown in Fig. 7, where Li-rich giant stars are also indicated.

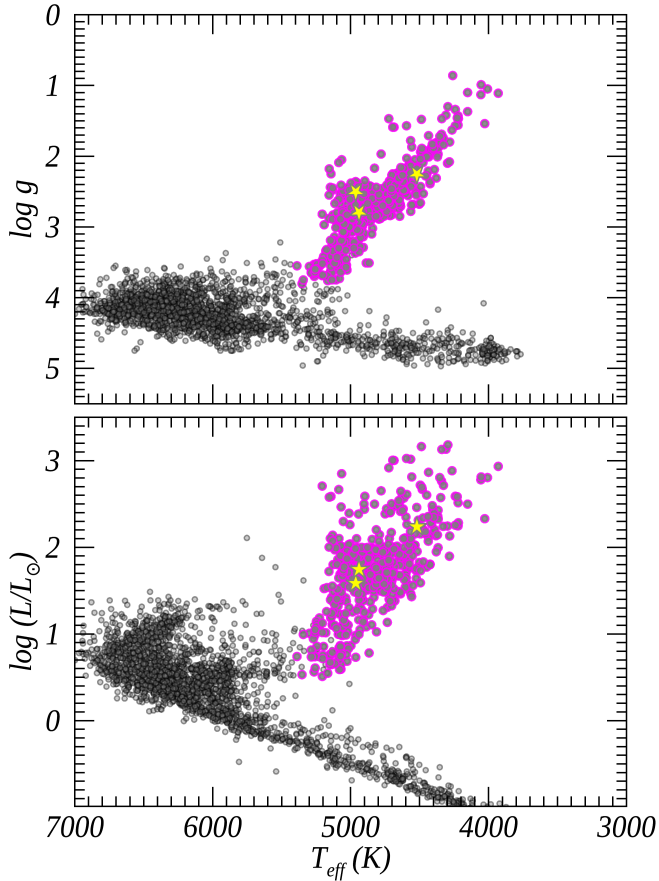


Fig. 5. Position in the HRD and the Kiel diagram of the members of the open clusters in *Gaia*-ESO IDR6 with age ≥ 130 Myr selected in this study. MS and sub-giant stars are shown in black, and more evolved giants are plotted in magenta. The Li-rich stars are marked with yellow stars.

Table 1. Summary of the selected samples.

Sample	Stars with A(Li)	Detections
<i>Gaia</i> -ESO IDR6	38 090	27 256
<i>Gaia</i> -ESO IDR6 + <i>Gaia</i> DR3	37 940	27 142
Field stars	7369	3866
Cluster members	4212	3497

To improve the quality of the sample, we cross-matched our catalogue with *Gaia* EDR3 and selected only stars for which the parallaxes have uncertainties within 10%. We computed the stellar luminosity for these stars using the geometric distances from Bailer-Jones et al. (2021) and the *Gaia* EDR3 G magnitudes, converted into V magnitudes using the G_{BP} and G_{RP} colours. We computed the bolometric magnitudes using the bolometric corrections BC(K), based on the $V-K$ colours² from the tables provided by Alonso et al. (1999) for dwarf and giant stars. We used bolometric corrections based on colour instead of more recent calibrations, such as that of Casagrande & Vandenberg (2018), based on stellar parameters, in order to provide corrections independent of stellar parameters, which can have considerably large uncertainties, especially for the GIRAFFE spectra, because the

² K magnitudes are obtained from the 2MASS catalogue (Skrutskie et al. 2006).

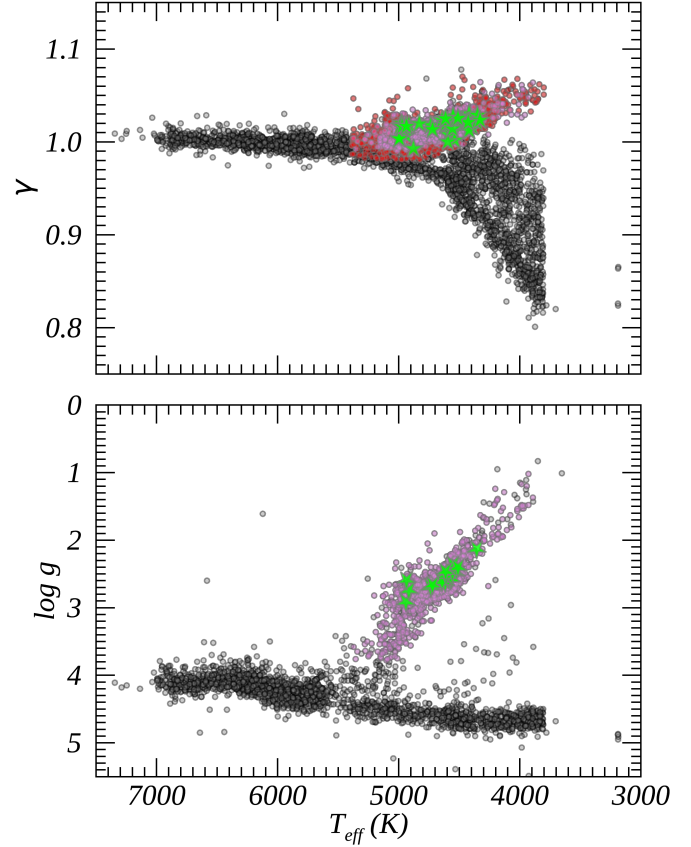


Fig. 6. Selection of giant stars in the Milky Way field as non-members of young clusters, in the γ vs. T_{eff} diagram (upper panel) and in the Kiel diagram (bottom panel). Giants selected on the basis of the T_{eff} and $\log g$ criterion are shown in pink, those selected on the basis of the T_{eff} and γ criterion are shown in red, and MS and PMS stars are marked in black. The Li-rich giant stars are indicated with green stars.

spectral range of HR15N is not optimised to derive precise atmospheric parameters, and to be able to apply them also to stars for which we have γ instead of $\log g$. We adopted the reddening values from the 3D extinction map of Green et al. (2019), extracting $E(B-V)$ in the line of sight and at the distance of each star, when available, and from the 2D extinction map of Schlegel et al. (1998) in the remaining cases. As expected, $E(B-V)$ from Schlegel et al. (1998) is typically larger than $E(B-V)$ from Green et al. (2019), the latter being integrated over larger distances. We took as an estimate of $E(B-V)$ the minimum of the two values, which is equivalent to using Green et al. (2019) when it is available, and excluded stars with $E(B-V) > 1$. For Li-rich giant stars, we relaxed the selection on parallax by removing the cuts on the parallax relative error to avoid losing some of them. The final sample for which we have high-quality luminosities from *Gaia*, with error on $\log(L/L_{\odot})$ lower than 0.15 dex, contains 7369 stars, about 56% of which are giant stars (see Table 1). The stellar parameters (including γ), A(Li) (measurements and upper limits), and masses for the adopted sample of field stars are given in Table A.3.

The histogram of the distribution of [Fe/H] for the field stars is shown in Fig. 8. The peak of the metallicity distribution function (MDF) is at [Fe/H] ~ -0.1 , with a tail of lower-metallicity stars down to [Fe/H] ~ -1.0 , and of higher-metallicity stars reaching [Fe/H] $\sim +0.5$. In the inset of Fig. 8 we highlight the low-metallicity tail of the MDF: some stars have $-2.0 < [\text{Fe}/\text{H}] < -1.0$ and a few stars lie below [Fe/H] = -2.0 .

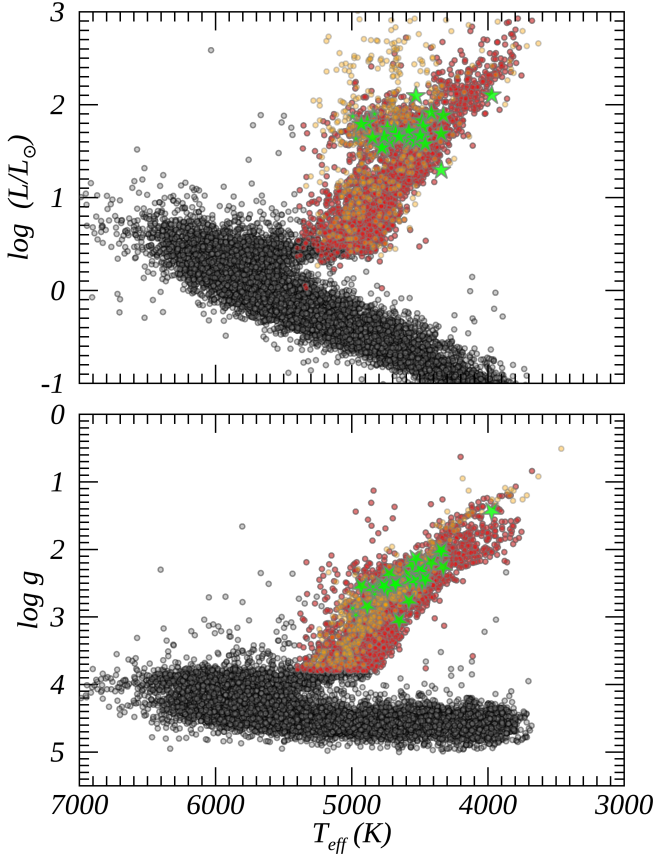


Fig. 7. Selection of giant stars in the Milky Way field as non-member of clusters with age > 130 Myr (orange) and in the field (red). In black we plot MS and sub-giant stars. *Upper panel:* HR diagram, *bottom panel:* Kiel diagram. In both panels, Li-rich giant stars are indicated by green stars.

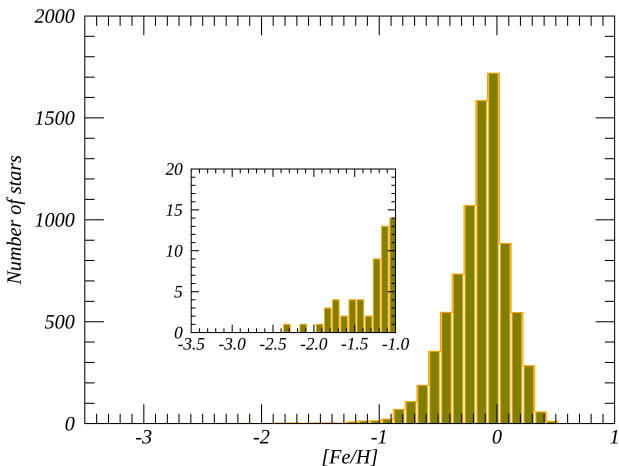


Fig. 8. Histogram of $[Fe/H]$ for the sample of field stars. In the inset we show the tail at low $[Fe/H]$.

3. Comparison with other catalogues

Gaia-ESO IDR6 has 676 stars in common with GALAH DR3 (Buder et al. 2021) with available Li abundances in both surveys. These stars belong to several different groups (not all are part of the selection discussed in this paper): the open clusters λ Ori, 25 Ori and Cha I, NGC 2243, NGC 2516, IC 4665, M 67, NGC 6253, Rup 147, Rup 7, Trumpler 20, the globular clusters

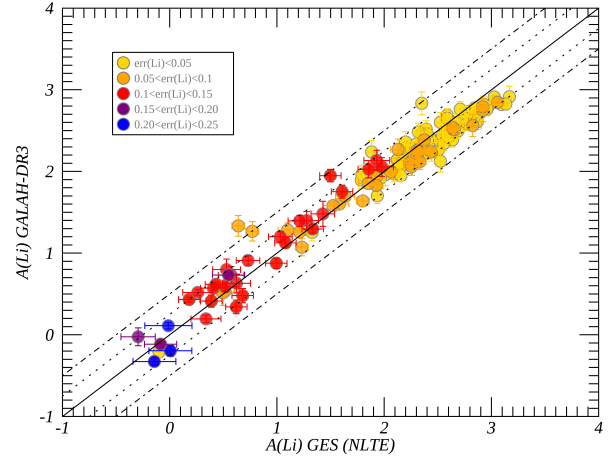


Fig. 9. $A(Li)$ corrected for 3D NLTE effects for stars in common between *Gaia*-ESO IDR6 (not all of them are part of our final selection) and GALAH DR3 (Buder et al. 2021). The circles are colour-coded by the error from *Gaia*-ESO in $A(Li)$. The continuous line is the one-to-one relation, the two dashed lines are at ± 0.5 dex, and the two dotted lines at ± 0.25 dex.

NGC 362 and NGC 104, several Milky Way field stars (mainly turn-off stars), and stars in the CoRoT and K2 fields. From the sample of stars in common, we selected a sub-sample of 135 stars with high-quality $A(Li)$ in both surveys: for *Gaia*-ESO, we took only Li measurements with an error lower than 0.25 dex for which we were able to compute NLTE corrections following Wang et al. (2021) for a meaningful comparison with GALAH NLTE Li abundances; from GALAH, we considered Li abundances with $flag_sp=0$ and $flag_li_fe=0$ (quality flags that indicate the good quality of the spectral analysis and of the $A(Li)$ determination, respectively), and an error lower than 0.25 dex. We recall that not all of the 135 stars are used here, but they were included for a general comparison of the two surveys. The comparison is shown in Fig. 9. The abundances are colour-coded according to the *Gaia*-ESO uncertainties. The lithium abundances in the two surveys agree very well. There is some scatter in the comparison, but in most cases, the agreement of *Gaia*-ESO and GALAH is within 0.25 dex.

We also compared stars in common between *Gaia*-ESO IDR6, to which we applied the NLTE corrections from Wang et al. (2021), and the AMBRE sample of Guiglion et al. (2016), considering the Li abundances corrected for NLTE effects (Lind et al. 2009) available in Guiglion et al. (2016). The agreement is quite good, with a small offset towards higher $A(Li)$ in the Guiglion et al. (2016) sample.

4. Post-MS lithium evolution: Comparison with stellar model predictions

The results of the recent studies using *Gaia* and large spectroscopic surveys (e.g. Deepak & Reddy 2019; Deepak et al. 2020; Charbonnel et al. 2020; Kumar & Reddy 2020; Yan et al. 2021) have been instructive for the understanding of the Li post-MS evolution. We here provide additional information for a better understanding of the MHD transport processes acting during the evolution of low- and intermediate-mass stars at different metallicities. With the *Gaia*-ESO results, we can indeed expand the analysis to a larger sample of stars in different metallicity ranges, thus investigating the Li evolution from the MSTO to the RGB sequence in different conditions. In particular, the combination

of field stars and of members of open clusters allow us to cover a wider range of stellar masses, from the lowest masses in field and old clusters to the highest masses in young open clusters.

In the following sections, we compare our results with a set of stellar models from [Lagarde et al. \(2012\)](#). The models were computed with the stellar evolution code STAREVOL (v3.00). The mechanisms included for the transport of chemicals are: (i) the standard mechanism due to convection. (ii) The thermohaline double-diffusive instability (so-called thermohaline mixing) that is expected to develop in low-mass stars along the RGB at the luminosity bump and in intermediate-mass stars on the early AGB. This occurs when in the external part of the hydrogen-burning shell around the degenerate stellar core, the mean molecular weight gradient in a thermalised medium is inverted ([Charbonnel & Zahn 2007](#); [Charbonnel & Lagarde 2010](#)). (iii) Rotation-induced mixing according to Zahn, with the vertical and horizontal turbulent coefficients from [Talon & Zahn \(1997\)](#) and [Zahn \(1992\)](#), respectively, computed considering a rotational velocity equal to 30% of the critical one at the zero-age MS, which means typical velocities on the MS between 90 and 137 km s⁻¹. In our comparison, we consider the classical models, in which only mixing due to convection is applied, and the models in which the effect of rotation-induced mixing and thermohaline mixing are included. We recall that these types of models are also crucial for an explanation of the behaviour of the Li abundance during the MS. Of the various considered additional mechanisms, rotation (see [Sestito & Randich 2005](#)) and overshooting mixing ([Christensen-Dalsgaard et al. 2011](#); [Zhang 2012](#)) have been introduced to reproduce the observational properties of the clusters and the properties of the Sun simultaneously. However, for low-mass solar-type stars with relatively extended convective envelopes, hydrodynamic processes induced by rotation, such as meridional circulation and shear mixing, predict large rotation gradients within the interior, which for instance require internal gravity waves or other mechanisms, such as penetrative convection, tachocline mixing, and additional turbulence to explain the rotation profile and the surface abundance of lithium in solar-type stars of various ages (see [Talon & Charbonnel 2005](#); [Dumont et al. 2021](#)).

4.1. Li evolution in field stars

Because stellar masses also play a fundamental role during the post-main sequence evolution, we estimated them to compare with the appropriate theoretical models from [Lagarde et al. \(2012\)](#). Masses of field stars were computed using the maximum likelihood technique described in [Charbonnel et al. \(2020\)](#) that was adapted from [Valle et al. \(2014\)](#), with which we compared T_{eff} , luminosity, and [Fe/H] of individual stars with the theoretical evolutionary tracks of [Lagarde et al. \(2012\)](#). The errors on the three parameters were taken into account to estimate the uncertainty on the stellar mass. In Fig. 10 we show the HR diagram of our sample of giant and sub-giant field stars (see Sect. 2.2 for a definition), divided into four metallicity bins, and overlaid on the corresponding evolutionary tracks from [Lagarde et al. \(2012\)](#). Most of our stars are located in the ascending and upper parts of the RGB and in the clump.

In Fig. 11 we show the evolution of A(Li) as a function of the effective temperature in three mass bins: $M \leq 1.8 M_{\odot}$, $1.8 M_{\odot} < M \leq 2.2 M_{\odot}$, and $M > 2.2 M_{\odot}$. Each mass bin is further divided into the four metallicity bins [Fe/H] ≤ -0.5 , $-0.5 < [\text{Fe}/\text{H}] \leq -0.1$, $-0.1 < [\text{Fe}/\text{H}] \leq +0.1$, and [Fe/H] $> +0.1$. In the panels, we show both sub-giant and giant stars. When available in our samples, we also include MSTO stars (at the

responding mass and metallicity) with $T_{\text{eff}} > 6200$ K that might have preserved their initial Li, as expected in the classical models. We compare the observations with the theoretical predictions of the models of [Lagarde et al. \(2012\)](#); classical and with thermohaline and rotation-induced mixings).

Figure 11 shows that the Li surface evolution predicted by classical models is very similar for stars of different masses and metallicities. In this case, the surface Li depletion is only due to the FDU, which starts at T_{eff} around 5600 K. Because for low-mass stars the maximum depth reached by the base of the convective envelope during the FDU is almost independent of the stellar mass, A(Li) reaches similar values for all models of the same metallicity: A(Li) ~ 1.3 – 1.6 dex at solar metallicity, and A(Li) ~ 0.7 – 1.0 dex for the sub-solar models at [Fe/H] = -0.56 . These values agree with previous theoretical studies (starting e.g. with the early work of [Iben 1967](#)). After the end of the FDU (around $T_{\text{eff}} \sim 5000$ – 4500 K, depending on the mass and metallicity), the convective envelope withdraws in mass, and no more surface Li depletion is expected.

As already mentioned in the introduction (see references to previous studies in Sect. 1) and shown in Fig. 11, these classical predictions do not reproduce the observed Li behaviour. For the masses and metallicities explored here, Li depletion starts earlier (i.e. at higher T_{eff}) on the subgiant branch than predicted by the classical models, and it is more efficient. Additionally, the second depletion episode that occurs in stars with masses below $\sim 2.2 M_{\odot}$ after the so-called RGB luminosity bump (at $T_{\text{eff}} \sim 4200$ K, i.e. when the H-burning shell has passed the chemical discontinuity left behind by the FDU) is not predicted either by the classical stellar evolution theory.

The Li data for field stars presented in Fig. 11 thus confirm the need of including in stellar evolution models rotation-induced mixing over the entire considered mass and metallicity range, as well as thermohaline mixing in low-mass stars that pass through the RGB bump before igniting He in their degenerate core at the tip of the RGB. On one hand, rotation-induced mixing changes the abundances profile in the stellar interiors already during the main sequence, enlarging the size of the Li-free region. As a consequence, compared to classical predictions, surface Li depletion starts earlier (i.e. at higher T_{eff}), and lower Li abundances are predicted after the end of the FDU ([Palacios et al. 2003](#); [Charbonnel et al. 2020](#)).

Figure 11 clearly shows that rotating models reproduce the Li abundance from the MSTO on, regardless of the mass and metallicity ranges. On the other hand, the introduction in the models of the thermohaline double diffusive instability as proposed by [Charbonnel & Zahn \(2007\)](#) reconciles the theoretical predictions with the Li data in the brightest and coolest RGB stars. When these low-mass evolved stars pass the RGB bump, this instability develops between the base of the convective envelope and the Li-burning regions because of the mean molecular weight inversion resulting from the ${}^3\text{He}({}^3\text{He}, 2p){}^4\text{He}$ reaction in the hydrogen-burning shell.

As already shown with other samples from the literature ([Charbonnel & Zahn 2007](#); [Charbonnel & Lagarde 2010](#); [Lagarde et al. 2015](#); [Charbonnel et al. 2020](#)), this explains the second drop of the surface Li abundance that is highlighted by the *Gaia*-ESO field star data shown in Fig. 11. Inside stars more massive than $\sim 2.2 M_{\odot}$, however, the thermohaline instability does not set in because they do not pass through the RGB bump: they ignite central helium-burning earlier in non-degenerate conditions. For this mass range (panels in the right column of Fig. 11), the lowest observed Li abundances are clearly explained by rotation alone, as discussed before.

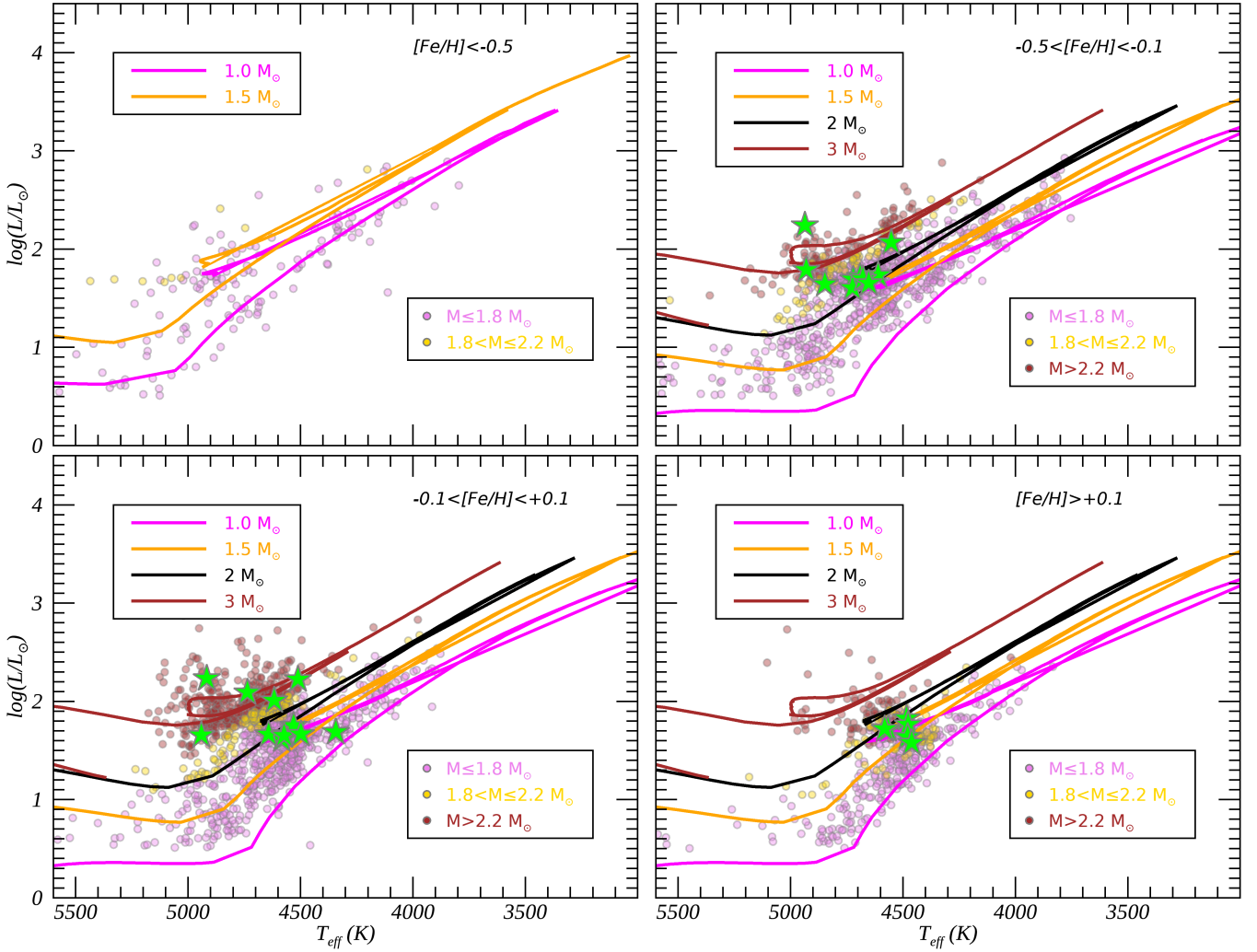


Fig. 10. Location of our sample of sub-giant and giant field stars in the HR diagram in the four metallicity bins. The stars (filled circles) are colour-coded by their masses: in pink we show stars with $M \leq 1.2 M_{\odot}$, in yellow we plot stars with $1.2 M_{\odot} < M \leq 2.2 M_{\odot}$, and in red we show stars with $M > 2.2 M_{\odot}$. The Li-rich giant stars with a mass determination are marked with green stars. The theoretical evolutionary tracks are plotted for masses between 1 and $3 M_{\odot}$. In the *top left panel*, corresponding to the metallicity bin with $[\text{Fe}/\text{H}] \leq -0.5$, we adopt the tracks computed for $[\text{Fe}/\text{H}] = -0.56$, while in the other bins we plot the tracks at the solar metallicity.

Finally, Fig. 11 shows a conspicuous number of giant stars with an anomalously high $A(\text{Li})$ with respect to the general trend discussed above. Some of them, from the previous *Gaia*-ESO data releases, have been studied in detail by Casey et al. (2016) and Smiljanic et al. (2018). We discuss them in Sect. 5.

4.2. Li evolution in open clusters

Lithium abundances in open clusters provide an effective way to probe mixing processes in stars of different masses and metallicity, following them through the different evolutionary sequences. Because the ages of open clusters can be derived with good accuracy from the isochrone fitting of their whole evolutionary sequence, we can estimate the masses of their evolved stars by assuming them to be those of the MSTO stars. Moreover, high-resolution spectra provide a detailed chemical composition for the cluster, which usually has a high level of homogeneity (see e.g. De Silva et al. 2006; Carrera & Martínez-Vázquez 2013; Bovy 2016; Liu et al. 2016).

In this way, stars in open clusters might effectively serve to study the changes in Li abundance during post-MS evolution in

samples with similar masses and metallicity. Several works have been dedicated to the study of the evolution of Li abundance in specific parts of the colour-magnitude diagrams (CMD) of open clusters. Some works (Randich et al. 2002, 2007; Smiljanic et al. 2010; Canto Martins et al. 2011; Pace et al. 2012; Anthony-Twarog et al. 2018; Deliyannis et al. 2019) studied Li abundance in MS, sub-giant stars, and RGB stars in several open clusters, finding that non-standard mixing processes are needed to explain the observed trends. Other papers focused on Li in RGB stars and on the occurrence of Li-rich giants in open clusters (see e.g. Anthony-Twarog et al. 2013; Monaco et al. 2014; Delgado Mena et al. 2016; Krolikowski et al. 2016; Aguilera-Gómez et al. 2016; Carlberg et al. 2015, 2016).

We present a large sample of stars here, members of 57 open clusters, with $0.13 \text{ Gyr} < \text{ages} < 7 \text{ Gyr}$, spanning from the inner disc to the outer Galaxy, with R_{GC} in the range $\sim 6\text{--}20 \text{ kpc}$, and with metallicities $-0.44 \text{ dex} < [\text{Fe}/\text{H}] < +0.27 \text{ dex}$. In Figs. 12 and 13 we plot $A(\text{Li})$ vs. T_{eff} for the 34 clusters of our sample in which $A(\text{Li})$ was measured in six giant stars at least. For clusters with ages between 130 and 2000 Myr we indicate the initial $A(\text{Li})$ that we derive from the analysis of upper MS stars

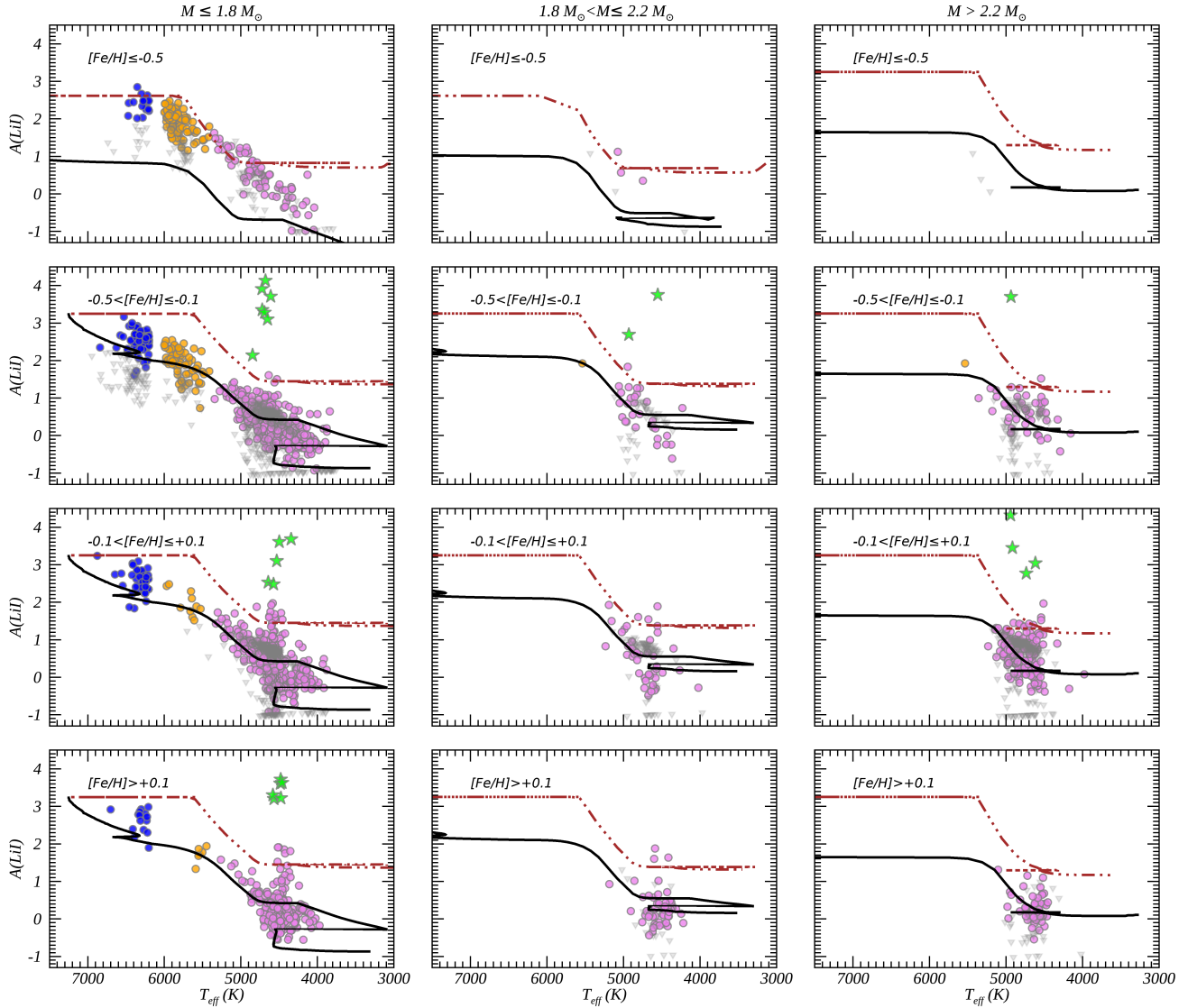


Fig. 11. $A(\text{Li})$ vs. T_{eff} in the field stars sample for which the mass was estimated. We plot in blue the MSTO stars (with $T_{\text{eff}} > 6200$ K), in orange the sub-giant stars, and in pink the giant stars. Li upper limits are shown with grey triangles. The curves are the predictions of the models of Lagarde et al. (2012) for $1.5 M_{\odot}$, $2.0 M_{\odot}$, and $3.0 M_{\odot}$ with standard mixing (dashed lines) and with rotation-induced mixing and thermohaline instability (continuous lines). In the panels for $[\text{Fe}/\text{H}] < -0.5$ dex and $M \leq 2.2 M_{\odot}$, we adopt the models at $[\text{Fe}/\text{H}] = -0.56$, and in the other panels the models at $[\text{Fe}/\text{H}] = 0$. The Li-rich stars with a mass determination are indicated with green stars.

located on the blue side of the so-called Li dip when possible, following the method described in Randich et al. (2020). For NGC 2420 and NGC 2243, given their ages, stars on the blue side of the dip are located at the upper TO (see also François et al. 2013). Because they may have started to experience some post-MS Li dilution, the measured Li might be a lower limit to their initial value. We compared the observations with the evolutionary tracks from the models of Lagarde et al. (2012), as for the field stars. For each cluster we selected the most appropriate model in terms of stellar mass, using the MSTO masses in Table A.1. We adopted models at solar metallicity for all clusters because the cluster $[\text{Fe}/\text{H}]$ are closer to the solar ones than to the next metallicity in the grid of Lagarde et al. (2012).

For the youngest cluster NGC 6067 (age = 130 Myr), the RGB stars reach $A(\text{Li}) \sim 1$ dex in Fig. 12, which is in between the tracks of the classical model and the model with rotation at $4 M_{\odot}$ (these models were scaled to -0.6 dex in $A(\text{Li})$ to match the initial Li of the cluster). In slightly older clusters with $190 \text{ Myr} < \text{age} \leq 400$ Myr, namely NGC 6259, NGC 6705, and NGC 3532,

the lithium in RGB stars reaches $A(\text{Li}) \sim 1$ – 1.2 dex, following the track of $3 M_{\odot}$, which is in between the classical ones and those with rotation. For the clusters in Fig. 12 with an age in the range $400 \text{ Myr} < \text{age} \leq 1400$ Myr, from NGC 6802 to NGC 6005, in the RGB stars $A(\text{Li})$ settles between 0 dex and 1 dex. These clusters are compared with tracks of $2 M_{\odot}$ stars, where the effects of both rotation-induced mixing and thermohaline instability are required to reproduce the decline of $A(\text{Li})$ with decreasing T_{eff} . Cluster ages in the interval $1400 \text{ Myr} < \text{age} \leq 6800$ Myr are compared with tracks for $1.5 M_{\odot}$ stars (starting from NGC 4437 in Fig. 12 to Berkeley 36 in Fig. 13). For all these clusters, the data are also better reproduced by the models that include the effects of rotation-induced mixing and thermohaline instability. Starting from clusters with age > 1500 Myr (NGC 2158), $A(\text{Li})$ in RGB stars reaches lower values, down to $A(\text{Li}) \sim -1$ dex because the efficiency of the thermohaline instability increases. However, for the lowest-mass range, corresponding to ages > 4000 Myr, the comparison should be taken with caution. In the

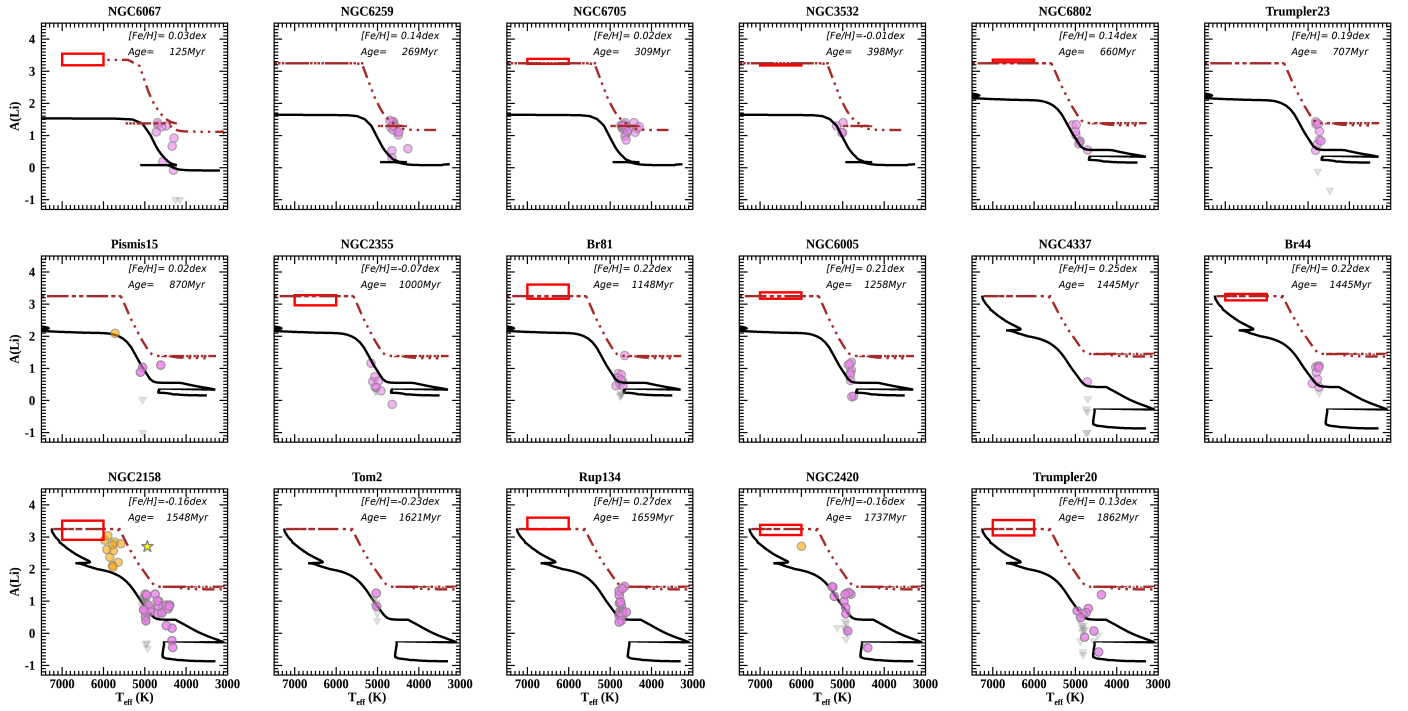


Fig. 12. A(Li) vs. T_{eff} for 17 *Gaia*-ESO clusters with ages ≤ 1.8 Gyr. Giant stars are indicated with pink circles, stars with upper limits of A(Li) are shown with grey triangles, sub-giants are indicated with orange circles, and Li-rich giants are marked with yellow stars. The red rectangles show the location of the initial A(Li), derived as in [Randich et al. \(2020\)](#). The theoretical tracks of [Lagarde et al. \(2012\)](#) are selected on the basis of the age and metallicity of each cluster (classical models are shown with dot-dashed brown curves, and rotation-induced mixing models with continuous black curves). Cluster metallicity and age are reported in each panel.

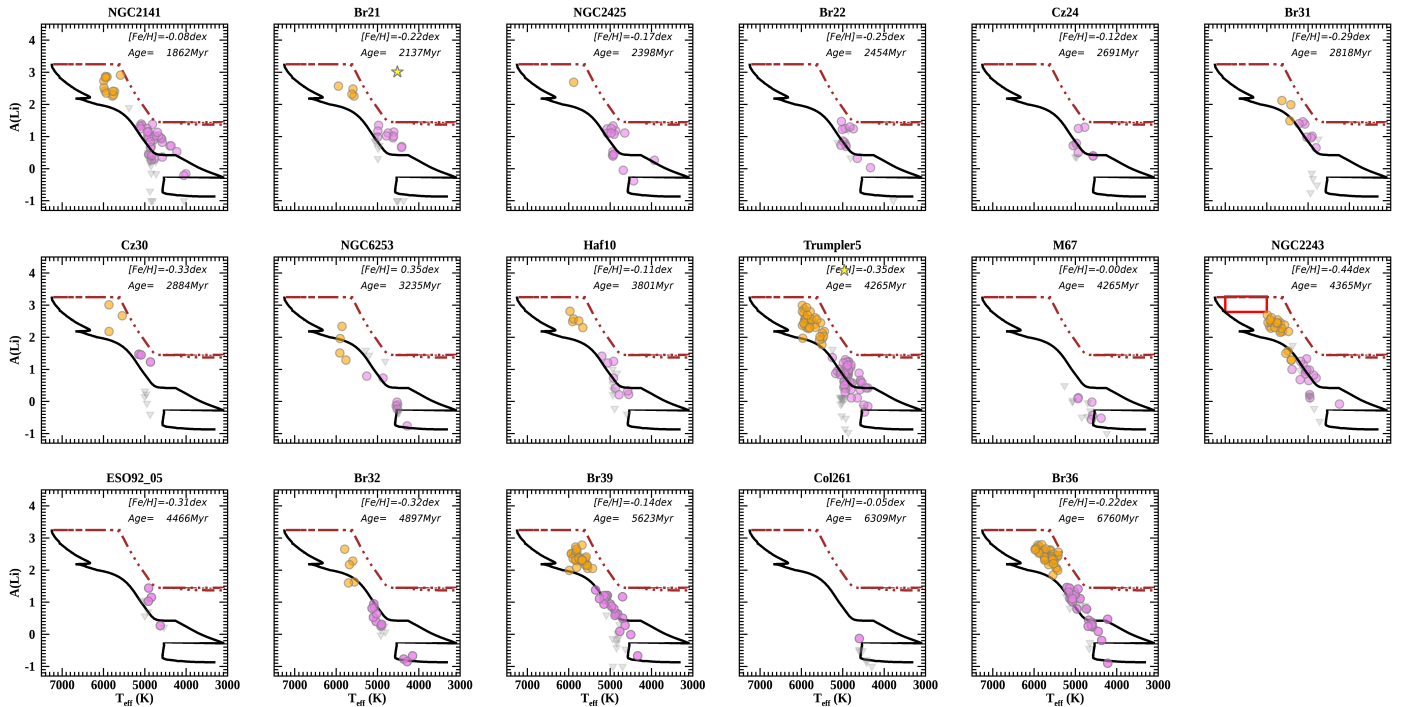


Fig. 13. A(Li) vs. T_{eff} for the remaining *Gaia*-ESO clusters with age ≥ 1.8 Gyr. Colours and symbols are the same as in Fig. 12.

[Lagarde et al. \(2012\)](#) models, the transport of angular momentum is driven by meridional circulation and turbulence alone, while an additional transport is required to explain the internal rotation profile of low-mass stars on the MS (see references in [Dumont et al. 2021](#), for the case of the Sun and solar-type stars)

and along the red giant branch (e.g. [Eggenberger et al. 2019](#), and references therein). For this reason, we compare the observations also for the oldest clusters with the model for $1.5 M_{\odot}$.

In Fig. 14 we compare the predictions of the stellar evolutionary models with the cluster data, binned by age. This

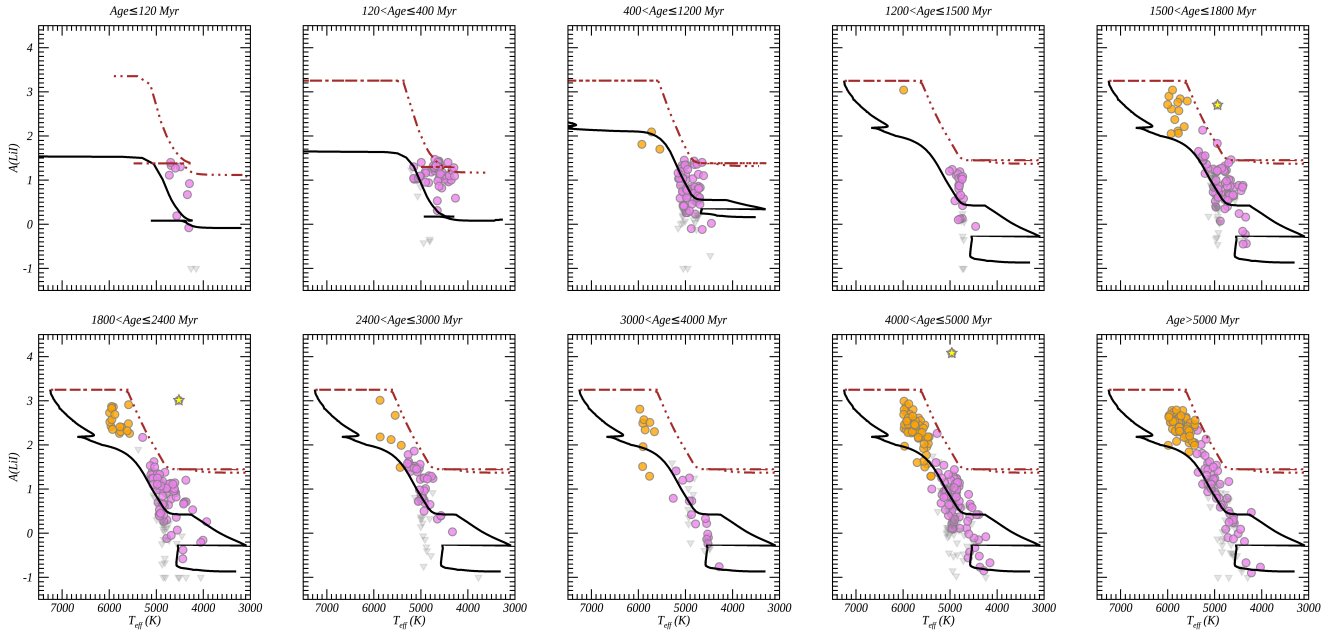


Fig. 14. $A(\text{Li})$ vs. T_{eff} in open clusters in different age bins. The curves are the model predictions from Lagarde et al. (2012) for the closest stellar masses, with standard mixing (dashed brown line) and including rotation-induced mixing (continuous black line), and for solar metallicity. Colours and symbols are the same as in Fig. 12.

allows us to re-introduce the cluster member stars that were not included in Figs. 12 and 13 because these clusters are too sparsely populated, and to have statistically significant samples in each age bin. We reach the same conclusions as in Sect. 4.1. In the highest-mass regime, corresponding to $130 \leq \text{age} \leq 400$ Myr, the strongest effect is rotation, which produces earlier and larger Li depletion than predicted by the classical model. In the clusters with $400 \text{ Myr} \leq \text{age} \leq 1200$ Myr, the rotation-induced mixing is needed to explain the behaviour of the lithium surface abundance in sub-giant and giant stars, while as the age increases (hence the stellar mass decreases), the effect of the thermohaline mixing starts to play a role and can explain, together with the rotation-induced mixing, the further decrease in $A(\text{Li})$ for ages > 1200 Myr. This effect is even stronger at ages > 4000 Myr.

5. Lithium-rich giant stars

In this section we discuss Li-rich giant stars that are found in open clusters and in the field. We recall the adopted definition of Li-rich giants: $A(\text{Li}) \geq 2.0$ dex, $3800 \text{ K} \leq T_{\text{eff}} \leq 5000 \text{ K}$, $\log g \leq 3.5$ or $\log(L/L_{\odot}) \geq 1$ dex and $\gamma \geq 0.98$. While red giant stars should have usually a lower Li surface abundance than in the previous evolutionary phases (see, however, Kumar et al. 2020, and Magrini et al., in prep.), some of them present a clear Li overabundance with respect to the bulk. A number of possible processes have been considered in the literature to explain the Li enrichment in these rare stars. Some works call for Li production through deep internal transport processes (e.g. Sackmann & Boothroyd 1999; Palacios et al. 2001; Cassisi et al. 2016). The Li enrichment has also been attributed to possible external pollution, such as planet engulfment or pollution by a binary companion (see e.g. the case of Li-rich *K* giant, Holanda et al. 2020) or to magnetic activity (Gonçalves et al. 2020). The ingestion of a planet or a companion brown dwarf can indeed contribute to an increase in angular momentum of the system, producing additional Li (see e.g. Alexander 1967; Siess & Livio 1999; Denissenkov & Weiss 2000; Carlberg et al.

2010; Aguilera-Gómez et al. 2016; Delgado Mena et al. 2016). The possible effects include an increase in the Li surface abundance and a change in the global metallicity and in rotational velocity (see e.g. Casey et al. 2016). Recently, several works have shown pollution of Be and Li in white dwarfs, likely due to accretion of icy exomoons that formed around giant exoplanets or of other rocky bodies in exoplanetary systems (Klein et al. 2021; Doyle et al. 2021; Kaiser et al. 2021). Other works, such as Jorissen et al. (2020), found that the binary frequency appears normal among the Li-rich giants, excluding a causal relation of Li enrichment and binarity.

5.1. Lithium-rich giant stars and their evolutionary status

The recent discovery of large samples of Li-rich giants indicates that they are not just restricted to the luminosity bump on the RGB for the low-mass stars, or its equivalent on the early-AGB for intermediate-mass stars that ignite central He burning in non-degenerate conditions (Charbonnel & Balachandran 2000). They are also found along the RGB and in the red clump (see e.g. Alcalá et al. 2011; Kumar et al. 2011; Lebzelter et al. 2012; Carlberg et al. 2016; Smiljanic et al. 2018; Deepak & Reddy 2019; Charbonnel et al. 2020; Kumar & Reddy 2020; Martell et al. 2021; Yan et al. 2021). Kumar & Reddy (2020), Yan et al. (2021), Singh et al. (2021) and Deepak & Lambert (2021), combining the results from asteroseismic and spectroscopic surveys, suggested that a high fraction of the Li-rich giants belongs to the red clump central He-burning phase, confirming a previous idea presented by Kumar et al. (2011). Similar results were obtained by Casey et al. (2019): 80% of their sample stars have likely helium-burning cores.

About 2% of our giant stars in the field are Li-rich stars (considering giants in the same temperature range as the Li-rich stars as a reference sample), while the percentage of Li-rich stars in open clusters is lower, 0.5%. These numbers agree with those found in several other surveys, which have reported the discovery of Li-rich giants in proportion of ~ 1 –2% of their total

Table 2. Red giant Li-rich stars in the field.

CNAME	Field	SETUP	T_{eff}	$\log g$	[Fe/H]	$v \sin i$	A(Li)	Other detection
06490710-2359450	Be 75 (non member)	HR15N	4993 ± 60	2.9 ± 0.2	-0.29 ± 0.05	≤ 7.0	2.19 ± 0.08	–
18182698-3242584	Bulge	U580	4340 ± 30	2.06 ± 0.06	0.06 ± 0.05	9.0	3.68 ± 0.05	Smiljanic et al. (2018)
18181062-3246291	Bulge	U580	4580 ± 30	2.37 ± 0.05	0.06 ± 0.05	8.0	2.01 ± 0.05	Smiljanic et al. (2018)
18033785-3009201	Bulge	U580	4480 ± 30	2.48 ± 0.05	0.13 ± 0.05	8.0	3.61 ± 0.04	Smiljanic et al. (2018)

Notes. The full table is available online at the CDS.

sample (see e.g. Brown et al. 1989; Charbonnel & Balachandran 2000; Lèbre et al. 2006; Kumar et al. 2011; Casey et al. 2016; Smiljanic et al. 2018; Deepak & Reddy 2019; Charbonnel et al. 2020).

In the field sample, we find 71 Li-rich giant stars, selected both with the criterion based on the gravity index γ (21 stars) and with the surface gravity (50 stars). For giant stars with only γ there might still be some contamination with PMS stars. They are listed in Table 2, where we present their properties: their CNAME, GES field, SETUP, the stellar parameters, $v \sin i$, A(Li) measured in the present work, and detection in previous works. Of the 50 stars selected through their $\log g$, we recovered 35 of the 40 Li-rich giants presented in Casey et al. (2016) and Smiljanic et al. (2018). The remaining 5 stars have A(Li) slightly below 2.0 dex in IDR6, and thus they do not appear in our list of Li-rich giants with A(Li) ≥ 2.0 dex. The sample contains stars in the direction of the Bulge, 23 stars in the Corot fields (3 new discoveries) and one in the Kepler2 field, and stars in the field of several open clusters that are non-members.

In Fig. 15 we show their location in the Kiel diagram, displaying only those with available $\log g$. Our data show no immediate correspondence of Li-rich stars to the position of the red clump, but instead we see a distribution around three main locations: the red giant branch luminosity bump, the core He-burning stages, or the early-asymptotic giant branch, as discussed for a sub-sample of these stars in Smiljanic et al. (2018). As discussed by these authors, one of the CoRoT targets, 101167637 (CNAME=19265193+0044004), is a confirmed He-core burning clump giant. Their full characterisation with asteroseismology would thus be necessary to reliably determine the evolutionary status of each Li-rich star.

The three Li-rich giants detected as members of open clusters are listed in Table 3, in which we give their properties: CNAME, the host cluster, the setup used to measure A(Li), stellar parameters, $v \sin i$, and A(Li), and are shown in Fig. 15 with a different symbol. They belong to Trumpler 5, Berkeley 21, and NGC 2158. The star in Trumpler 5 was first identified by Monaco et al. (2014), who attributed the Li enrichment to internal production that occurred at the red clump or in the immediately preceding phases. The star in Berkeley 21 was discovered by Hill & Pasquini (1999), who measured its high Li content and related it to internal processes, but did not discard the possibility of accretion from external sources. The Li-rich giant in NGC 2158 is, to our knowledge, a new detection. Two of the three Li-rich stars are located close to the RC; one of them is at the beginning of the RGB luminosity bump. They do not have an enhanced rotational velocity, as would be expected if the Li-enrichment were related to planet engulfment, for example (see e.g. Privitera et al. 2016, and the discussion in Sec 5.2).

5.2. Li abundance and rotational velocity

The relation of rotation and lithium abundance in evolved stars is not yet completely established (see e.g. Wallerstein et al. 1994;

de Medeiros et al. 1997, 2000; de Laverny et al. 2003; Mallik et al. 2003). As discussed in Smiljanic et al. (2018), fast rotation during the giant phase cannot be explained by single-star evolution and might be related to planet engulfment (Alexander 1967; Carlberg et al. 2009, 2010; Casey et al. 2016; Privitera et al. 2016; Anthony-Twarog et al. 2020). Following Privitera et al. (2016), the planet engulfment might have a strong effect on the Li abundances, even for a limited portion of the giant life. However, the effect is difficult to distinguish from other processes that can modify the Li abundance because Li is a fragile element, is easily destroyed, and is subject to other mechanisms of production during the red giant phase. Delgado Mena et al. (2016) searched for Li-rich giants in a sample of clusters that was searched for planets and derived A(Li) abundances in 12 open clusters. They studied the relation of $v \sin i$ and A(Li) and reported that the giant stars with higher A(Li) have higher rotation velocities than the Li-depleted stars. However, they also found that the relation might reflect the different evolutionary status of their sample stars, with the hottest stars having higher rotation rates.

For our sample of giant stars in the field and in clusters, we sought possible correlations between A(Li) and the projected rotational velocities. In a conservative way, we considered as fast-rotating giant stars those with $v \sin i > 10 \text{ km s}^{-1}$. In our sample, the instrumental limit prevented us from measuring $v \sin i \leq 7 \text{ km s}^{-1}$, therefore we can provide only an upper limit for them. The results are shown in Fig. 16, where we plot A(Li) as a function of the projected rotational velocity for giants with $3800 \text{ K} \leq T_{\text{eff}} \leq 5000 \text{ K}$ and $\log g \leq 3.5$, both Li-rich (A(Li) ≥ 2) and normal giants. The samples of giant stars observed by de Medeiros et al. (2000) and by Delgado Mena et al. (2016) are over-plotted for comparison. We note a trend of increasing A(Li) with increasing $v \sin i$. However, for $10 \text{ km s}^{-1} \leq v \sin i \leq 30 \text{ km s}^{-1}$, we observe stars with A(Li) both above and below 2.0 dex. Many Li-rich stars have low $v \sin i$, including the three Li-rich stars in open clusters, indicating that the preferential way to produce Li enrichment in giant stars is related to some specific phases of stellar evolution, as shown in Fig. 15, and that the correlation with the projected rotational velocity indicates that lithium enrichment by engulfment is an occasional effect.

6. Summary and conclusions

We exploited a sample of giant stars with Li measurements in *Gaia*-ESO IDR6 to investigate the evolution of A(Li) from the MSTO to the giant phase. We combined the *Gaia*-ESO data with *Gaia* EDR3 to obtain the distances and stellar luminosities. We compared our lithium abundances with literature values and found a good agreement.

We selected MS, sub-giant, and giant stars that are member stars of open clusters and field stars. We studied the general trends of lithium abundances after the MS. Because

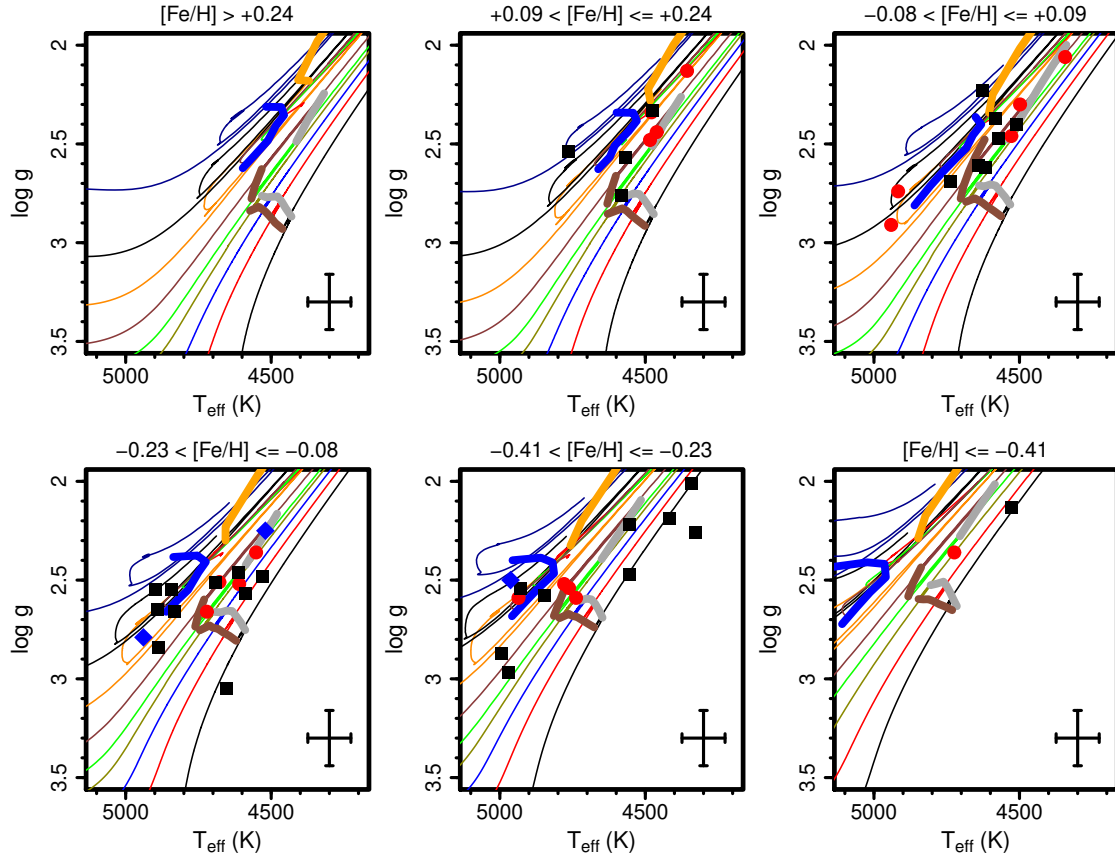


Fig. 15. Kiel diagram of the Li-rich ($A(\text{Li}) \geq 2.0$ dex) giant stars compared with PARSEC evolutionary tracks (Bressan et al. 2012; Fu et al. 2018) of masses 0.8, 1.0, 1.2, 1.4, 1.5, 1.7, 2.0, 2.4, and $3.0 M_{\odot}$. From the top left to the bottom right panels: the models have $[\text{Fe}/\text{H}] = +0.30, +0.18, 0.00, -0.15, -0.30,$ and -0.52 dex. The range of $[\text{Fe}/\text{H}]$ of the stars is given at the top of each panel. Field stars with $A(\text{Li}) \geq 3.3$ dex are shown as red circles, while stars with $2.0 \text{ dex} \leq A(\text{Li}) < 3.3$ dex are marked with black squares. The three Li-rich stars in open clusters are shown as blue diamonds. The beginning and end of the RGB luminosity bump are marked as thick grey and brown lines, respectively. The position of the clump of low-mass giants is shown as a thick blue line (from 0.8 to $1.9 M_{\odot}$). The beginning of the early-AGB of intermediate-mass stars ($\geq 2.0 M_{\odot}$) is highlighted as the thick orange line. Typical error bars are shown in the bottom right corner of the panels.

Table 3. Red giant Li-rich stars in open clusters.

CNAME	Clusters	SETUP	T_{eff}	$\log g$	$[\text{Fe}/\text{H}]$	$v \sin i$	A(Li)	Other detection
06364020+0929478	Trumpler 5	U580	4960 ± 30	2.50 ± 0.05	-0.37 ± 0.04	≤ 7.0	4.08 ± 0.05	Monaco et al. (2014)
05514200+2148497	Be 21	U580	4520 ± 30	2.25 ± 0.05	-0.18 ± 0.04	≤ 7.0	3.01 ± 0.06	Hill & Pasquini (1999)
06072443+2400524	NGC 2158	HR15N	4940 ± 60	2.8 ± 0.2	-0.17 ± 0.06	≤ 7.0	2.70 ± 0.09	–

stellar masses play a fundamental role during the post-main sequence evolution, we selected samples of stars with reliable measurements of stellar masses: member stars of open clusters (age > 130 Myr), and field stars with masses derived from isochrone fitting. Our data probe, with a homogeneous analysis, lithium abundances and stellar parameters for stars with a wide range of stellar masses, covered thanks to the sample of young and intermediate-age open clusters (with MSTO masses from 1.1 to $4.5 M_{\odot}$) that are not usually available in surveys that account only for field stars.

We compared our results with the set of stellar models of Lagarde et al. (2012), in which the effect of rotation-induced mixing and thermohaline instability are included. The comparison of our data and model results confirmed the strong effect of the rotation-induced mixing already in massive stars. The lower-mass giant stars in clusters and in the field also provide support to the hypothesis that a mixing process in advanced phases

of stellar evolution is required, which might be thermohaline mixing. We confirm the agreement of data and models with rotation-induced and thermohaline mixing in the whole mass and metallicity ranges.

We discussed the properties of our Li-rich sample of stars, including both field stars and a few members of open clusters. They are distributed around three main locations in the Kiel diagram: the red giant branch luminosity bump, the core-He burning stages, and the early-asymptotic giant branch. Their full characterisation with asteroseismology is required to establish a unique link with the evolutionary status of each star. Finally, we investigated possible effects of the residual stellar rotation, after the MS, during the giant phase. We find only a few stars with $v \sin i > 10 \text{ km s}^{-1}$, and their Li abundance is in line with the other stars in the same evolutionary state. We do not find any conclusive correlation between Li-rich stars and the projected rotational velocity.

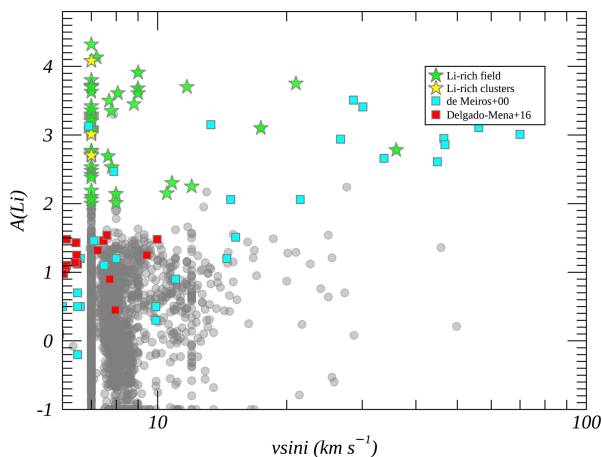


Fig. 16. $A(\text{Li})$ as a function of the projected rotational velocity, $v \sin i$, in our sample of giant stars with $3800 \text{ K} \leq T_{\text{eff}} \leq 5000 \text{ K}$ and $\log g \leq 3.5$: grey circles are the giant stars in open clusters and in the field with $A(\text{Li}) < 2.0$ dex, while light yellow and green stars represent $A(\text{Li}) \geq 2$ dex in giants in open clusters and in the field, respectively. Red squares are the giant stars observed by Delgado Mena et al. (2016), and cyan squares are those observed by de Medeiros et al. (2000).

Acknowledgements. We thank the referee for her/his careful reading of the paper, and for comments, which improved the quality of the work and its presentation. Based on data products from observations made with ESO Telescopes at the La Silla Paranal Observatory under programme ID 188.B-3002. These data products have been processed by the Cambridge Astronomy Survey Unit (CASU) at the Institute of Astronomy, University of Cambridge, and by the FLAMES/UVES reduction team at INAF/Osservatorio Astrofisico di Arcetri. These data have been obtained from the *Gaia*-ESO Survey Data Archive, prepared and hosted by the Wide Field Astronomy Unit, Institute for Astronomy, University of Edinburgh, which is funded by the UK Science and Technology Facilities Council. This work was partly supported by the European Union FP7 programme through ERC grant number 320360 and by the Leverhulme Trust through grant RPG-2012-541. We acknowledge the support from INAF and Ministero dell' Istruzione, dell' Universit  e della Ricerca (MIUR) in the form of the grant "Premiale VLT 2012". The results presented here benefit from discussions held during the *Gaia*-ESO workshops and conferences supported by the ESF (European Science Foundation) through the GREAT Research Network Programme. LM, GC, SR, MVdS acknowledges the funding from MIUR Premiale 2016: MITiC. MVdS, LM and AV thank the WEAVE-Italia consortium. LM acknowledges the funding from the INAF PRIN-SKA 2017 program 1.05.01.88.04. NL acknowledges the "Programme National de Physique Stellaire" (PNPS) and the "Programme National Cosmologie et Galaxies (PNCG)" of CNRS/INSU co-funded by CEA and CNES. CVV and LM thank the COST Action CA18104: MW-*Gaia*. LS acknowledges financial support from the Australian Research Council (discovery Project 170100521) and from the Australian Research Council Centre of Excellence for All Sky Astrophysics in 3 Dimensions (ASTRO 3D), through project number CE170100013. TB acknowledges financial support by grant No. 2018-04857 from the Swedish Research Council. EDM acknowledges the support from Funda o para a Ci ncia e a Tecnologia (FCT) through the research grants UIDB/04434/2020 and UIDP/04434/2020 and by the Investigador FCT contract IF/00849/2015. FJE acknowledges financial support from the Spanish MINECO/FEDER through the grant AYA2017-84089 and MDM-2017-0737 at Centro de Astrobiolog a (CSIC-INTA), Unidad de Excelencia Mar a de Maeztu, and from the European Union's Horizon 2020 research and innovation programme under Grant Agreement no. 824064 through the ESCAPE – The European Science Cluster of Astronomy and Particle Physics ESFRI Research Infrastructures project. ASB acknowledges the financial support of the STFC. E.D.M. acknowledges the support from Funda o para a Ci ncia e a Tecnologia (FCT) through national funds and from FEDER through COMPETE2020 by the grant UIDB/04434/2020 and UIDP/04434/2020 and by the Investigador FCT contract IF/00849/2015.

References

Aguilera-G mez, C., Chanam , J., Pinsonneault, M. H., & Carlberg, J. K. 2016, *ApJ*, **833**, L24
 Alcal , J. M., Biazzo, K., Covino, E., Frasca, A., & Bedin, L. R. 2011, *A&A*, **531**, L12

Alexander, J. B. 1967, *The Observatory*, **87**, 238
 Alonso, A., Arribas, S., & Mart nez-Roger, C. 1999, *A&AS*, **140**, 261
 Angelou, G. C., D'Orazi, V., Constantino, T. N., et al. 2015, *MNRAS*, **450**, 2423
 Anthony-Twarog, B. J., Deliyannis, C. P., Twarog, B. A., Croxall, K. V., & Cummings, J. D. 2009, *AJ*, **138**, 1171
 Anthony-Twarog, B. J., Deliyannis, C. P., Rich, E., & Twarog, B. A. 2013, *ApJ*, **767**, L19
 Anthony-Twarog, B. J., Deliyannis, C. P., Harmer, D., et al. 2018, *AJ*, **156**, 37
 Anthony-Twarog, B. J., Deliyannis, C. P., & Twarog, B. A. 2020, *AJ*, **160**, 75
 Asplund, M., Grevesse, N., Sauval, A. J., & Scott, P. 2009, *ARA&A*, **47**, 481
 Bailer-Jones, C. A. L., Rybizki, J., Foesneau, M., Demleitner, M., & Andrae, R. 2021, *AJ*, **161**, 147
 Balachandran, S. 1990, *ApJ*, **354**, 310
 Balachandran, S. 1995, *Mem. Soc. Astron. Ital.*, **66**, 387
 Baraffe, I., Pratt, J., Goffrey, T., et al. 2017, *ApJ*, **845**, L6
 Bensby, T., & Lind, K. 2018, *A&A*, **615**, A151
 Bovy, J. 2016, *ApJ*, **817**, 49
 Bravi, L., Zari, E., Sacco, G. G., et al. 2018, *A&A*, **615**, A37
 Bressan, A., Marigo, P., Girardi, L., et al. 2012, *MNRAS*, **427**, 127
 Brown, J. A., Sneden, C., Lambert, D. L., & Dutchover, E., Jr. 1989, *ApJS*, **71**, 293
 Buder, S., Sharma, S., Kos, J., et al. 2021, *MNRAS*, **506**, L50
 Cantat-Gaudin, T., Anders, F., Castro-Ginard, A., et al. 2020, *A&A*, **640**, A1
 Canto Martins, B. L., L bre, A., Palacios, A., et al. 2011, *A&A*, **527**, A94
 Carlberg, J. K., Majewski, S. R., & Arras, P. 2009, *ApJ*, **700**, 832
 Carlberg, J. K., Smith, V. V., Cunha, K., Majewski, S. R., & Rood, R. T. 2010, *ApJ*, **723**, L103
 Carlberg, J. K., Smith, V. V., Cunha, K., et al. 2015, *ApJ*, **802**, 7
 Carlberg, J. K., Cunha, K., & Smith, V. V. 2016, *ApJ*, **827**, 129
 Carrera, R., & Mart nez-V zquez, C. E. 2013, *A&A*, **560**, A5
 Casagrande, L., & Vandenberg, D. A. 2018, *MNRAS*, **479**, L102
 Casey, A. R., Ruchti, G., Masseron, T., et al. 2016, *MNRAS*, **461**, 3336
 Casey, A. R., Ho, A. Y. Q., Ness, M., et al. 2019, *ApJ*, **880**, 125
 Cassisi, S., Salaris, M., & Pietrinfermi, A. 2016, *A&A*, **585**, A124
 Castro, M., Duarte, T., Pace, G., & do Nascimento, J. D. 2016, *A&A*, **590**, A94
 Ceillier, T., Eggenberger, P., Garc a, R. A., & Mathis, S. 2013, *A&A*, **555**, A54
 Charbonneau, P., & Michaud, G. 1990, *ApJ*, **352**, 681
 Charbonnel, C., & Balachandran, S. C. 2000, *A&A*, **359**, 563
 Charbonnel, C., & Lagarde, N. 2010, *A&A*, **522**, A10
 Charbonnel, C., & Zahn, J. P. 2007, *A&A*, **467**, L15
 Charbonnel, C., Brown, J. A., & Wallerstein, G. 1998, *A&A*, **332**, 204
 Charbonnel, C., Lagarde, N., Jasniewicz, G., et al. 2020, *A&A*, **633**, A34
 Christensen-Dalsgaard, J., Monteiro, M. J. P. F. G., Rempel, M., & Thompson, M. J. 2011, *MNRAS*, **414**, 1158
 Coc, A., Vangioni-Flam, E., Descouvemont, P., Adahchour, A., & Angulo, C. 2004, *ApJ*, **600**, 544
 Damiani, F., Prisinzano, L., Micela, G., et al. 2014, *A&A*, **566**, A50
 de Laverny, P., do Nascimento, J. D., L bre, A., & De Medeiros, J. R. 2003, *A&A*, **410**, 937
 de Laverny, P., Recio-Blanco, A., Worley, C. C., & Plez, B. 2012, *A&A*, **544**, A126
 de Medeiros, J. R., do Nascimento, J. D., & Mayor, M. 1997, *A&A*, **317**, 701
 de Medeiros, J. R., do Nascimento, J. D., Sankaranakutty, S., Costa, J. M., & Maia, M. R. G. 2000, *A&A*, **363**, 239
 De Silva, G. M., Sneden, C., Paulson, D. B., et al. 2006, *AJ*, **131**, 455
 Deal, M., Richard, O., & Vauclair, S. 2021, *A&A*, **646**, A160
 Deepak, & Lambert, D. L. 2021, *MNRAS*, **505**, 642
 Deepak, & Reddy, B. E. 2019, *MNRAS*, **484**, 2000
 Deepak, Lambert, D. L., & Reddy, B. E. 2020, *MNRAS*, **494**, 1348
 Delgado Mena, E., Tsantaki, M., Sousa, S. G., et al. 2016, *A&A*, **587**, A66
 Deliyannis, C. P., Pinsonneault, M. H., & Charbonnel, C. 2000, *IAU Symp.*, **198**, 61
 Deliyannis, C. P., Anthony-Twarog, B. J., Lee-Brown, D. B., & Twarog, B. A. 2019, *AJ*, **158**, 163
 Denissenkov, P. A., & Tout, C. A. 2003, *MNRAS*, **340**, 722
 Denissenkov, P. A., & Weiss, A. 2000, *A&A*, **358**, L49
 Denissenkov, P. A., Pinsonneault, M., & MacGregor, K. B. 2009, *ApJ*, **696**, 1823
 Doyle, A. E., Desch, S. J., & Young, E. D. 2021, *ApJ*, **907**, L35
 Dumont, T., Palacios, A., Charbonnel, C., et al. 2021, *A&A*, **646**, A48
 Eggenberger, P., Haemmerl , L., Meynet, G., & Maeder, A. 2012, *A&A*, **539**, A70
 Eggenberger, P., Lagarde, N., Miglio, A., et al. 2017, *A&A*, **599**, A18
 Eggenberger, P., Deheuvels, S., Miglio, A., et al. 2019, *A&A*, **621**, A66
 Franciosini, E., Sacco, G. G., Jeffries, R. D., et al. 2018, *A&A*, **616**, L12
 Fran ois, P., Pasquini, L., Biazzo, K., Bonifacio, P., & Palsa, R. 2013, *A&A*, **552**, A136
 Fu, X., Bressan, A., Marigo, P., et al. 2018, *MNRAS*, **476**, 496
 Gaia Collaboration (Brown, A. G. A., et al.) 2021, *A&A*, **649**, A1

- Galli, D., & Palla, F. 2013, *ARA&A*, 51, 163
- Garaud, P. 2021, ArXiv e-prints [arXiv:2103.08072]
- Garaud, P., & Kulenthirarajah, L. 2016, *ApJ*, 821, 49
- Gilmore, G., Randich, S., Asplund, M., et al. 2012, *The Messenger*, 147, 25
- Gonçalves, B. F. O., da Costa, J. S., de Almeida, L., Castro, M., & do Nascimento, J. D. 2020, *MNRAS*, 498, 2295
- Gonzalez, O. A., Zoccali, M., Monaco, L., et al. 2009, *A&A*, 508, 289
- Gratton, R. G., Sneden, C., Carretta, E., & Bragaglia, A. 2000, *A&A*, 354, 169
- Green, G. M., Schlafly, E., Zucker, C., Speagle, J. S., & Finkbeiner, D. 2019, *ApJ*, 887, 93
- Grisoni, V., Matteucci, F., Romano, D., & Fu, X. 2019, *MNRAS*, 489, 3539
- Guiglion, G., de Laverny, P., Recio-Blanco, A., et al. 2016, *A&A*, 595, A18
- Henkel, K., Karakas, A. I., & Lattanzio, J. C. 2017, *MNRAS*, 469, 4600
- Hill, V., & Pasquini, L. 1999, *A&A*, 348, L21
- Holanda, N., Drake, N. A., & Pereira, C. B. 2020, *MNRAS*, 498, 77
- Iben, I., Jr. 1967, *ApJ*, 147, 624
- Jackson, R. J., Jeffries, R. D., Lewis, J., et al. 2015, *A&A*, 580, A75
- Jorissen, A., Van Winckel, H., Siess, L., et al. 2020, *A&A*, 639, A7
- Kaiser, B. C., Clemens, J. C., Blouin, S., et al. 2021, *Science*, 371, 168
- Klein, B., Doyle, A. E., Zuckerman, B., et al. 2021, *ApJ*, 914, 61
- Krolikowski, D. M., Steinhauer, A. J., Deliyannis, C. P., Twarog, B. A., & Anthony-Twarog, B. J. 2016, *AAS Meeting Abstracts*, 227, 240.30
- Kumar, Y. B., & Reddy, B. E. 2020, *JApA*, 41, 49
- Kumar, Y. B., Reddy, B. E., & Lambert, D. L. 2011, *ApJ*, 730, L12
- Kumar, Y. B., Reddy, B. E., Campbell, S. W., et al. 2020, *Nat. Astron.*, 4, 1059
- Lagarde, N., Decressin, T., Charbonnel, C., et al. 2012, *A&A*, 543, A108
- Lagarde, N., Miglio, A., Eggenberger, P., et al. 2015, *A&A*, 580, A141
- Lambert, D. L., Dominy, J. F., & Sivertsen, S. 1980, *ApJ*, 235, 114
- Lanzafame, A. C., Frasca, A., Damiani, F., et al. 2015, *A&A*, 576, A80
- Lattanzio, J. C., Siess, L., Church, R. P., et al. 2015, *MNRAS*, 446, 2673
- Lèbre, A., de Laverny, P., Do Nascimento, J. D., & de Medeiros, J. R. 2006, *A&A*, 450, 1173
- Lebzelter, T., Utenthaler, S., Busso, M., Schultheis, M., & Aringer, B. 2012, *A&A*, 538, A36
- Lind, K., Primas, F., Charbonnel, C., Grundahl, F., & Asplund, M. 2009, *A&A*, 503, 545
- Liu, F., Asplund, M., Yong, D., et al. 2016, *MNRAS*, 463, 696
- Mallik, S. V., Parthasarathy, M., & Pati, A. K. 2003, *A&A*, 409, 251
- Marques, J. P., Goupil, M. J., Lebreton, Y., et al. 2013, *A&A*, 549, A74
- Martell, S., Simpson, J., Balasubramaniam, A., et al. 2021, *MNRAS*, 505, 5340
- Mathis, S. 2013, in *Transport Processes in Stellar Interiors*, eds. M. Goupil, K. Belkacem, C. Neiner, F. Lignières, & J. J. Green, 865, 23
- Mathis, S., Prat, V., Amard, L., et al. 2018, *A&A*, 620, A22
- Matteucci, F., D'Antona, F., & Timmes, F. X. 1995, *A&A*, 303, 460
- Michaud, G. 1986, *ApJ*, 302, 650
- Monaco, L., Boffin, H. M. J., Bonifacio, P., et al. 2014, *A&A*, 564, L6
- Olive, K. A. 2013, *AIP Conf. Ser.*, 1560, 314
- Pace, G., Castro, M., Meléndez, J., Théado, S., & do Nascimento, J. D. 2012, *A&A*, 541, A150
- Palacios, A., Charbonnel, C., & Forestini, M. 2001, *A&A*, 375, L9
- Palacios, A., Talon, S., Charbonnel, C., & Forestini, M. 2003, *A&A*, 399, 603
- Palmerini, S., Cristallo, S., Busso, M., et al. 2011, *ApJ*, 741, 26
- Pancino, E., Lardo, C., Altavilla, G., et al. 2017, *A&A*, 598, A5
- Pasquini, L., Randich, S., Zoccali, M., et al. 2004, *A&A*, 424, 951
- Pitrou, C., Coc, A., Uzan, J.-P., & Vangioni, E. 2018, *Phys. Rep.*, 754, 1
- Prantzos, N. 2012, *A&A*, 542, A67
- Prat, V., & Lignières, F. 2013, *A&A*, 551, L3
- Prat, V., Lignières, F., & Lagarde, N. 2015, *SF2A-2015: Proceedings of the Annual meeting of the French Society of Astronomy and Astrophysics*, 419
- Privitera, G., Meynet, G., Eggenberger, P., et al. 2016, *A&A*, 593, A128
- Randich, S., & Magrini, L. 2021, *Frontiers Astron. Space Sci.*, 8, 6
- Randich, S., Primas, F., Pasquini, L., & Pallavicini, R. 2002, *A&A*, 387, 222
- Randich, S., Primas, F., Pasquini, L., Sestito, P., & Pallavicini, R. 2007, *A&A*, 469, 163
- Randich, S., Gilmore, G., & Gaia-ESO Consortium. 2013, *The Messenger*, 154, 47
- Randich, S., Tognelli, E., Jackson, R., et al. 2018, *A&A*, 612, A99
- Randich, S., Pasquini, L., Franciosini, E., et al. 2020, *A&A*, 640, L1
- Richard, D., & Zahn, J.-P. 1999, *A&A*, 347, 734
- Richard, O., Vauclair, S., Charbonnel, C., & Dziembowski, W. A. 1996, *A&A*, 312, 1000
- Roccatagliata, V., Sacco, G. G., Franciosini, E., & Randich, S. 2018, *A&A*, 617, L4
- Romano, D., Matteucci, F., Ventura, P., & D'Antona, F. 2001, *A&A*, 374, 646
- Sacco, G. G., Morbidelli, L., Franciosini, E., et al. 2014, *A&A*, 565, A113
- Sackmann, I. J., & Boothroyd, A. I. 1999, *ApJ*, 510, 217
- Schlegel, D. J., Finkbeiner, D. P., & Davis, M. 1998, *ApJ*, 500, 525
- Schramm, D. N., Steigman, G., & Dearborn, D. S. P. 1990, *ApJ*, 359, L55
- Sengupta, S., & Garaud, P. 2018, *ApJ*, 862, 136
- Sestito, P., & Randich, S. 2005, *A&A*, 442, 615
- Siess, L., & Livio, M. 1999, *MNRAS*, 308, 1133
- Singh, R., Reddy, B. E., Campbell, S. W., Bharat Kumar, Y., & Vrad, M. 2021, *ApJ*, 913, L4
- Skrutskie, M. F., Cutri, R. M., Stiening, R., et al. 2006, *AJ*, 131, 1163
- Smiljanic, R. 2020, *Mem. Soc. Astron. Ital.*, 91, 142
- Smiljanic, R., Gauderon, R., North, P., et al. 2009, *A&A*, 502, 267
- Smiljanic, R., Pasquini, L., Charbonnel, C., & Lagarde, N. 2010, *A&A*, 510, A50
- Smiljanic, R., Korn, A. J., Bergemann, M., et al. 2014, *A&A*, 570, A122
- Smiljanic, R., Franciosini, E., Bragaglia, A., et al. 2018, *A&A*, 617, A4
- Somers, G., & Pinsonneault, M. H. 2016, *ApJ*, 829, 32
- Talon, S., & Charbonnel, C. 2005, *A&A*, 440, 981
- Talon, S., & Charbonnel, C. 2010, *IAU Symp.*, 268, 365
- Talon, S., & Zahn, J. P. 1997, *A&A*, 317, 749
- Tognelli, E., Prada Moroni, P. G., Degl'Innocenti, S., Salaris, M., & Cassisi, S. 2020, *A&A*, 638, A81
- Travaglio, C., Randich, S., Galli, D., et al. 2001, *ApJ*, 559, 909
- Valle, G., Dell'Omodarme, M., Prada Moroni, P. G., & Degl'Innocenti, S. 2014, *A&A*, 561, A125
- Wallerstein, G., Bohm-Vitense, E., Vanture, A. D., & Gonzalez, G. 1994, *AJ*, 107, 2211
- Wang, E. X., Nordlander, T., Asplund, M., et al. 2021, *MNRAS*, 500, 2159
- Yan, H.-L., Zhou, Y.-T., Zhang, X., et al. 2021, *Nat. Astron.*, 5, 86
- Zahn, J. P. 1992, *A&A*, 265, 115
- Zhang, Q. S. 2012, *MNRAS*, 427, 1441

- 1 INAF – Osservatorio Astrofisico di Arcetri, Largo E.Fermi, 5. 50125 Firenze, Italy
e-mail: laura.magrini@inaf.it
- 2 Institut UTINAM, CNRS UMR 6213, Univ. Bourgogne Franche-Comté, OSU THETA Franche-Comté-Bourgogne, Observatoire de Besançon, BP 1615, 25010 Besançon Cedex, France
- 3 Department of Astronomy, University of Geneva, Chemin de Pégase 51, 1290 Versoix, Switzerland
- 4 IRAP, UMR 5277 CNRS and Université de Toulouse, 14 Av. E.Belin, 31400 Toulouse, France
- 5 Nicolaus Copernicus Astronomical Center, Polish Academy of Sciences, ul. Bartycka 18, 00-716 Warsaw, Poland
- 6 Dipartimento di Fisica e Astronomia, Università degli Studi di Firenze, Via G. Sansone 1, 50019 Sesto Fiorentino, Firenze, Italy
- 7 Institute of Theoretical Physics and Astronomy, Vilnius University, Sauletekio Av. 3, 10257 Vilnius, Lithuania
- 8 INAF – Padova Observatory, Vicolo dell'Osservatorio 5, 35122 Padova, Italy
- 9 INAF – Rome Observatory, Via Frascati, 33, Monte Porzio Catone, Rome, Italy
- 10 ESO, Karl Schwarzschild Strasse 2, 85748 Garching, Germany
- 11 INAF – Osservatorio di Astrofisica e Scienza dello Spazio di Bologna, Via Gobetti 93/3, 40129 Bologna, Italy
- 12 Science and Technology Department, Parthenope University of Naples, Centro Direzionale, Isola C4, 80143 Naples, Italy
- 13 INAF – Osservatorio Astronomico di Capodimonte, Salita Moraliello, Napoli, Italy
- 14 INAF – Osservatorio Astronomico di Palermo, Piazza del Parlamento 1, 90134 Palermo, Italy
- 15 Dipartimento di Fisica “E.Fermi”, Università di Pisa, Largo Bruno Pontecorvo 3, 56127 Pisa, Italy
- 16 INFN, Sezione di Pisa, Largo Bruno Pontecorvo 3, 56127 Pisa, Italy
- 17 Departamento de Ciencias Físicas, Universidad Andres Bello, Fernandez Concha 700, Las Condes, Santiago, Chile
- 18 Université Côte d'Azur, Observatoire de la Côte d'Azur, CNRS, Laboratoire Lagrange, Nice, France
- 19 Instituto de Astrofísica e Ciências do Espaço, Universidade do Porto, CAUP, Rua das Estrelas, 4150-762 Porto, Portugal
- 20 Dipartimento di Fisica e Astronomia Galileo Galilei, Vicolo Osservatorio 3, 35122 Padova, Italy
- 21 Institute of Astronomy, University of Cambridge, Madingley Road, Cambridge CB3 0HA, UK

- ²² Departamento de Astrofísica, Centro de Astrobiología (CSIC-INTA), ESAC Campus, Camino Bajo del Castillo s/n, 28692 Villanueva de la Cañada, Madrid, Spain
- ²³ Núcleo de Astronomía, Facultad de Ingeniería y Ciencias, Universidad Diego Portales, Av. Ejército 441, Santiago, Chile
- ²⁴ Lund Observatory, Department of Astronomy and Theoretical Physics, Box 43, 221 00 Lund, Sweden
- ²⁵ GEPI, Observatoire de Paris, CNRS, Université Paris Diderot, 5 Place Jules Janssen, 92190 Meudon, France

- ²⁶ Leibniz-Institut für Astrophysik Potsdam (AIP), An der Sternwarte 16, 14482 Potsdam, Germany
- ²⁷ Instituto de Física y Astronomía, Facultad de Ciencias, Universidad de Valparaíso, Av. Gran Bretaña 1111, Valparaíso, Chile
- ²⁸ Núcleo Milenio Formación Planetaria – NPF, Universidad de Valparaíso, Av. Gran Bretaña 1111, Valparaíso, Chile
- ²⁹ Astrophysics Group, Keele University, Keele, Staffordshire ST5 5BG, UK
- ³⁰ Space Science Data Center – Agenzia Spaziale Italiana, Via del Politecnico, s.n.c., 00133 Rome, Italy

Appendix A: Additional tables

Table A.1. Parameters of our sample of open clusters from *Gaia*-ESO IDR6.

Id	Cluster	Age (Myr)	Distance (pc)	R_{GC} (kpc)	RV (km s ⁻¹)	[Fe/H] (dex)	MSTO (M_{\odot})	Parsec (Age _{iso} , Z _{iso}) (Gyr, Z)
1	NGC 6067	130	1880	6.8	-39.4 ± 0.2	0.03 ± 0.16	4.5	(0.13, 0.0145)
2	NGC 6709	190	1040	7.6	-11 ± 2	-0.03 ± 0.03	3.8	(0.2, 0.013)
3	Rup 7	230	5850	13.1	77 ± 1	-0.24 ± 0.04	3.4	(0.24, 0.007)
4	NGC 6192	240	1740	6.7	-8.1 ± 0.7	-0.08 ± 0.08	3.5	(0.24, 0.011)

Notes. ^(a)Only one star; ^(b)only stars with $\log g > 2.8$. The full table is available online at the CDS.

Table A.2. Sample of selected member stars in open clusters.

Id	Cluster	T_{eff} (K)	$\log g$	[Fe/H] (dex)	A(Li) (dex)	UL _{A(Li)} ^(a)	$\log(L/L_{\odot})$	γ	Mass (MSTO) (M_{\odot})
05323677+0011048	Br 20	4850 ± 30	2.70 ± 0.05	-0.32 ± 0.06	-0.02	1	1.64 ± 0.04	-	1.1
05323896+0011203	Br 20	4380 ± 30	1.81 ± 0.06	-0.43 ± 0.06	-0.63	1	2.13 ± 0.03	-	1.1
05512981+2143071	Br 21	6740 ± 60	4.3 ± 0.2	-0.37 ± 0.05	2.30 ± 0.25	0	1.29 ± 0.06	-	1.5
05515964+2144121	Br 21	6240 ± 80	4.1 ± 0.2	-0.28 ± 0.08	2.41	1	0.8 ± 0.1	-	1.5

Notes. ^(a)Upper limits are indicated with 1, detections with 0. The full table is available online at the CDS.

Table A.3. Sample of selected stars in the MW fields.

Id	GES_FLD	T_{eff} (K)	$\log g$	[Fe/H] (dex)	A(Li) (dex)	UL _{A(Li)} ^(a)	$\log(L/L_{\odot})$	γ	Mass (M_{\odot})
00000009-5455467	GES_MW_00_01	6060 ± 30	3.94 ± 0.05	-0.55 ± 0.05	2.34 ± 0.03	0	0.25 ± 0.02	-	0.8 ± 0.1
00000302-6002570	GES_MW_00_01	5780 ± 30	4.04 ± 0.05	-0.31 ± 0.04	2.01 ± 0.03	0	0.37 ± 0.01	-	0.9 ± 0.1

Notes. ^(a)Upper limits are indicated with 1, detections with 0. The full table is available online at the CDS.